nature communications

Article

https://doi.org/10.1038/s41467-025-57189-8

Mesoscale orchestration of collagen-based hierarchical mineralization

Received: 14 December 2023

Accepted: 14 February 2025

Published online: 27 February 2025

Check for updates

Minjuan Shen[1,2], Chunyan Zhang[1,2], Yangyang Zhang[1,2], Danyang Lu[1], Jian Yuan[1], Zhiyong Wang[1], Mengjie Wu[1], Mengqi Zhu[1] ✉ & Qianming Chen[1] ✉

Mesoscale building blocks are instrumental in bridging multilevel hierarchical mineralization, endowing macroscale entities with remarkable functionality and mechanical properties. However, the mechanism orchestrating the homogeneous morphology of mesoscale mineralized motifs in collagen-based hard tissues remains unknown. Here, utilizing avian tendons as a mineralization model, we reveal a robust correlation between the mesoscale mineralized spherules and the presence of phosvitin. By designing a phosvitin-stabilized biomineral cluster medium, we replicate the well-defined mesoscale spherical structure within collagen matrix in vitro and ex vivo. In-depth studies reveal that phosvitin undergoes a conformational transition in the presence of biominerals at physiological concentrations, and self-assembles into mineral-dense amyloid-like aggregates. The spatial binding of these mineral-dense aggregates to collagen serves as a template for guiding the formation of mineralized spherules on the mesoscale. On the nanoscale, this binding facilitates mineral precursor release and diffusion into the fibrils for intrafibrillar mineralization. This discovery underscores the pivotal role of phosvitin-biomineral aggregates in templating hierarchical mineralization from the mesoscale to the nanoscale. This study not only elucidates the intricate mechanism underlying the collagen-based mineralization hierarchy but also promotes a cutting-edge advance in highly biomimetic material design and regenerative medicine.

The sophisticated hierarchical architectures found in living organisms have captivated researchers for centuries. At the core of this fascination lies an inherent complexity and intricate programme that spans multiple length scales. Mesoscale, an intermediate level composed of nanoscale structural elements, endows macroscale entities with remarkable structural flexibility and functional versatility[1,2]. Similar to the hexagonal order of bee honeycombs and the teardrop-shaped rods of human enamel, mesoscale structures in nature have always fascinated scientists[3,4]. In vertebrate collagen-based biomineralization, the growth of mineral spherulites within the collagen matrix has been widely observed, leading to the formation of inorganic-organic spherical hybrid entities termed "mineralized spherules"[5–7]. These spherules function as mesoscale structural motifs that represent a new level of hierarchy, connecting nanoscale mineralized collagen fibrils with macroscale mineralized hard tissues[7,8]. To date, there has been little exploration of the hierarchical orchestration from nanoscale mineralized collagen fibrils into mesoscale mineralized spherules. Moreover, mechanisms underlying the regulation of mesoscale building blocks should be clarified. Unravelling the mesoscale orchestration that underlies collagen-based hierarchical mineralization would help

[1]Stomatology Hospital, School of Stomatology, Zhejiang University School of Medicine, Zhejiang Provincial Clinical Research Center for Oral Diseases, Key Laboratory of Oral Biomedical Research of Zhejiang Province, Engineering Research Center of Oral Biomaterials and Devices of Zhejiang Province, Hangzhou, China. [2]These authors contributed equally: Minjuan Shen, Chunyan Zhang, Yangyang Zhang. ✉e-mail: 7322022@zju.edu.cn; qmchen@zju.edu.cn

researchers better manipulate structure-function relationships in bioinspired material design[2].

To study the mesoscale mineralized spherules in-depth, an appropriate biomineralization model should be applied. Notably, the cascade of mineralization events in avian tendon biomineralization can be easily monitored spatially and temporally along collagen fibril bundles[6,9]. Thus, this system is suitable for exploring the intricate dynamics by which the mineralized spherules progressively form and their correlation with collagen fibrils. In tendons with normal mineralization, amorphous mineral precursors can be identified within the collagen matrix[9]. It has been widely acknowledged that noncollagenous proteins (NCPs), especially calcium-binding phosphoproteins, can stabilize amorphous calcium phosphate (ACP) precursors and thereby mediate intrafibrillar mineralization of collagen fibrils during biomineralization[10]. Early evidence showed that a heavily phosphorylated protein, phosvitin (Phov), can regulate ACP formation in avian embryo skeletal development[11]. However, the correlation between these components and hierarchical collagen-based mineralization, especially the formation of mesoscale mineralized spherules, has never been elucidated.

Notably, Phov is an intrinsically disordered protein (IDP)[12]. IDPs, such as dentin matrix protein 1 (DMP1) and amelogenin, can undergo conformational changes to guide crystal growth into a hierarchical structure[13,14]. The interplay between inorganic biominerals and functional organic moieties accelerates protein self-assembly, which is crucial for regulating the highly ordered mineralized structures[15]. Here, we hypothesize that the formation of mineralized spherules in collagen-based tissues, such as in mineralized avian tendons, might be orchestrated by Phov; by adopting a certain conformational organization under biomineral stimuli, Phov mediates collagen mineralization into distinctive hierarchical structures.

In this work, we conduct our research with a mineralized turkey tendon model. We find that mineralized spherules, incorporated with intrafibrillarly mineralized collagen fibrils and extrafibrillarly deposited minerals, exhibit a close association with Phov deposition at the mineralization front in vivo. Two-dimensional (2D) and 3D collagen-based models in vitro and ex vivo demonstrate that Phov could stabilize ACP precursors, mediate intra- and extra-fibrillar mineralization on the nanoscale, and reproduce highly biomimetic spherulitic structures on the mesoscale. During the dynamic mineralization process, we further observe that Phov-stabilized ACP (Phov-ACP) undergoes a conformational transformation and self-assembles into mineral-dense amyloid-like aggregates, which serve as mineralization templates for the formation of mineralized spherules on the mesoscale and for cross-fibrillar mineralization of collagen fibrils on the nanoscale. Interpreting the mechanisms underlying the mesoscale orchestration of Phov with mineralized spherules offers an innovative approach for highly biomimetic material design and promotes further advances in regenerative medicine.

Results and discussion

Mineralized spherules propagate in avian tendon mineralization

Avian gastrocnemius tendon was used to monitor the collagen mineralization process and identify the hierarchical mineralized structure at the mineralization front[9]. Micro-computed tomography (micro-CT) showed that the avian gastrocnemius tendons from 26-week-old turkeys were fully mineralized, while the 20-week-old turkeys' tendons were partially mineralized (Supplementary Fig. 2a, b). Histological examination of 20-week-old turkeys' tendons with haematoxylin & eosin and von Kossa staining (Supplementary Fig. 2c, d) further confirmed that mineral deposition predominantly occurred at the mineralization front.

To gain insight into the mineralization process and the mineral morphology at the mineralization front, longitudinal and transverse sections of the specimens were investigated by transmission electron microscopy (TEM). Parallel collagen fibril assembly was identifiable in TEM images (Fig. 1b). The rounded micrometre-sized electron-dense structures, which are termed mineralized spherules, were typically observed within the collagen matrix (Fig. 1c). With a higher mineral content, these spherules propagated and coalesced to achieve complete mineralization (Fig. 1d). In vertebrate biomineralization, mesoscale mineralized spherules have been recognized as a new hierarchy level in mineralized hard tissues[7,8]. Nevertheless, how these mineralized spherules form and grow within the collagen matrix remains elusive.

The natural mineralization process is regulated by strict biological control, endowing minerals with well-defined structures and variable functionalities[16]. Collagen fibrils serve as a protein scaffold for mineral growth. Particular NCPs, such as phosphoproteins, might regulate the morphology of mineralized structures[10]. Phov, the most heavily phosphorylated protein known to date[17], plays an important role in bone-like apatite formation. But it remains unclear whether phosphoproteins (mainly Phov) can induce the formation of mesoscale mineralized spherules during avian tendon mineralization. Accordingly, immunofluorescence staining and confocal laser scanning microscopy (CLSM) were used to investigate the spatial relationships between the mineralized matrix and Phov deposition by evaluating the superimposition of minerals, collagen fibrils and Phov in the calcifying region. Compared with nonmineralized turkey tendons (Fig. 1f), transverse and longitudinal tissue sections retrieved from mineralized tendon regions showed that Phov deposition was within the mineralized collagen matrix, especially in the region adjacent to the mineralization front (Fig. 1e). Immunofluorescence analysis also showed that the expression level of Phov was significantly higher within the calcifying region in the longitudinal and transverse growth directions ($P < 0.0001$) (Fig. 1g and Supplementary Fig. 3), indicating that Phov probably participates in the mineralization process. The Immunogold electron microscopy (immunogold-EM) technique was further used to ascertain the localization of Phov and mineralized spherules in the turkey tendon. Gold-labelled Phov was found to be deposited both inside and around the mineralized spherules, suggesting a close spatial relationship within mineralized tissues in vivo (Fig. 1h, i). Inside the internal structure of the mineralized spherule, intrafibrillarly mineralized collagen fibrils could be clearly observed. Mineralized collagen fibrils serve as an interlinked mineral network and a basic unit in spherical structures (Fig. 1c, d, h). Based on the spatial correlation observed between Phov and mineralized spherules, it was reasonable to examine whether Phov induces intrafibrillar collagen mineralization and regulates the growth of mineralized spherules to form hierarchically mineralized structures.

The formation of mineralized spherules is tightly controlled by phosvitin

To investigate this conundrum, Phov extracted from natural egg yolk (75 μg/mL) was used to stabilize supersaturated calcium phosphate (CaP) containing 3.5 mM $CaCl_2{\cdot}2H_2O$ and 2.1 mM K_2HPO_4. Cryo-transmission electron microscopy (cryo-TEM) was used to depict the structure of the Phov-CaP complex in the fully hydrated state. The freshly prepared Phov-CaP were electron-dense nanoparticles with an average diameter of 10.66 ± 1.43 nm (Fig. 2b and Supplementary Fig. 4). The selected area electron diffraction (SAED) pattern confirmed the amorphous nature of Phov-CaP (Fig. 2b). These data indicated that Phov can stabilize CaP into Phov-ACP.

To investigate whether Phov-ACP could induce collagen mineralization, self-assembled single collagen fibrils were reconstructed from rat tail-derived type I collagen and served as a 2D mineralization substrate. Cryo-TEM combined with SAED demonstrated a dense arrangement of needle-shaped crystals with the *c*-axis co-oriented along the long axis of the collagen fibril after 24 h of incubation with Phov-ACP (Fig. 2c). 3D reconstruction of cryo-TEM images also

https://doi.org/10.1038/s41467-025-57189-8

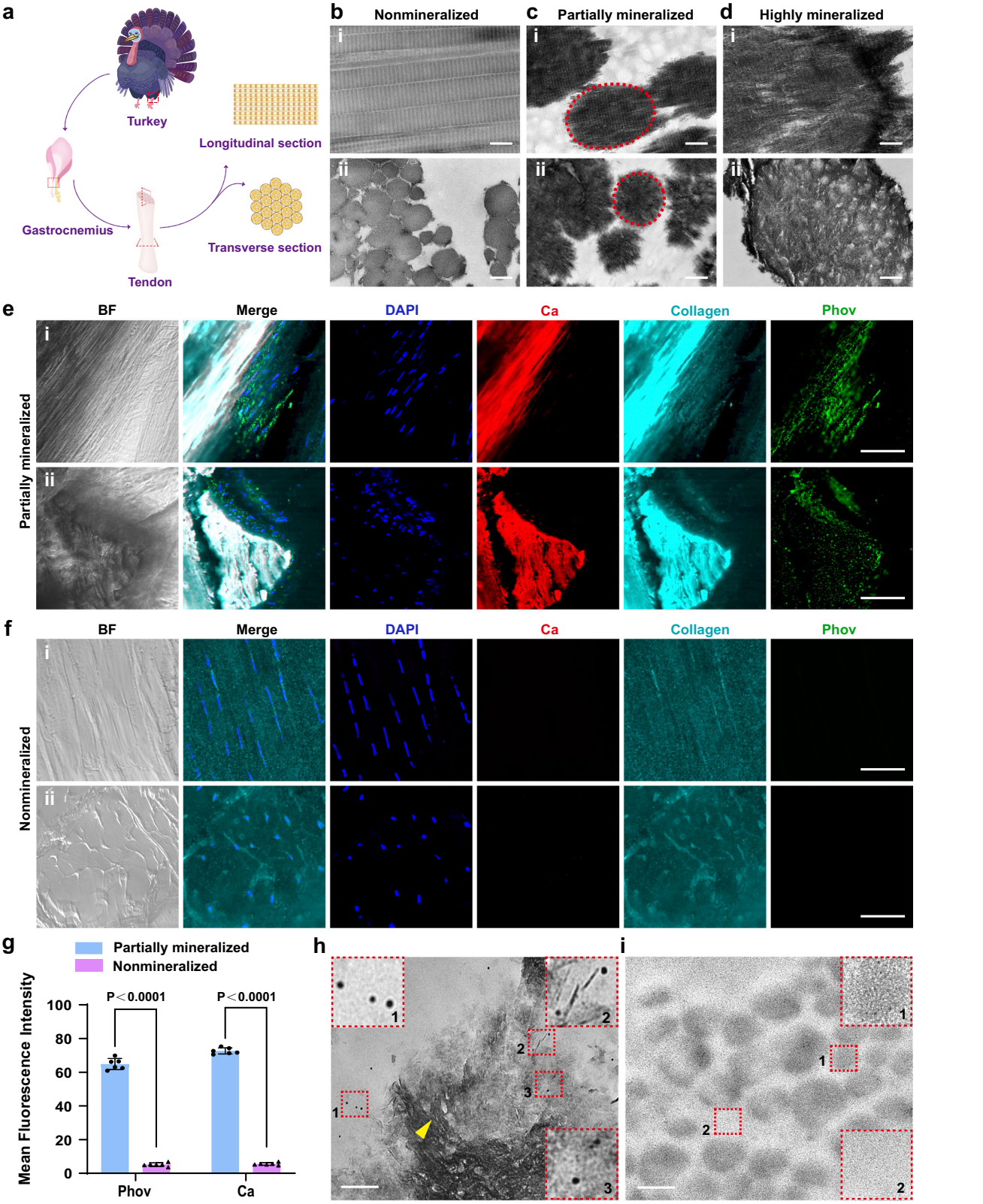

revealed substantial mineral deposition inside the collagen fibril, indicating a high degree of intrafibrillar mineralization (Supplementary Fig. 5 and Supplementary Movie 1).

To explore the Phov-ACP-mediated mineral deposition pattern within the collagen matrix, multi-layer collagen fibril membranes were used as 3D collagen matrix models. Focused ion beam scanning electron microscopy (FIB-SEM) showed that many roundish entities were formed within the collagen membrane after 48 h of mineralization (Fig. 2d). Energy dispersive spectrometry (EDS) mapping revealed calcium phosphate deposition within these circular structures, indicating the presence of mineralized spherules (Fig. 2e). High-magnification FIB-SEM images further demonstrated that intrafibrillar mineralized collagen fibrils, which were swelling yet exquisite, constructed the sophisticated mineralized spherules (Fig. 2d). This

https://doi.org/10.1038/s41467-025-57189-8

Fig. 1 | Mineralized spherule propagation and its correlation with phosvitin at the avian tendon mineralization front. a Scheme showing the preparation of turkey gastrocnemius tendons. **b**–**d** TEM images of longitudinal sections (**i**) and transverse sections (**ii**) of nonmineralized (**b**), partially mineralized (**c**) and highly mineralized (**d**) regions of avian tendons. Mineralized spherules are highlighted with red circles, with a typical spheroidal shape in the longitudinal section (**c-i**) and a circular profile in the transverse section (**c**–**ii**). In the highly mineralized region, heavily mineralized collagen could be identified (**d**). Scale bars: 300 nm. **e**, **f** Bright field and CLSM images of partially mineralized tendons (**e**) and nonmineralized tendons (**f**). In the partially mineralized tendon, Phov was deposited at the mineralization front in the longitudinal section (**e**–**i**) and transverse section (**e**–**ii**). Phov was virtually absent in the nonmineralized tendon both longitudinally (**f**–**i**) and transversely (**f**–**ii**). Blue, DAPI for nuclei; red, alizarin red S (ARS) for minerals; cyan, type I collagen; green, Phov; BF, bright field. Scale bars: 50 μm. **g** Semiquantitative analysis of calcium and Phov fluorescence intensities in longitudinal sections of partially mineralized and nonmineralized tendons. Data are presented as mean ± SD, $n = 6$ biologically independent samples, two-tailed unpaired t test (the P-values are shown). Differences with P-values < 0.05 are considered significant. **h**, **i** Immunogold-EM images showing Phov localization in the transverse sections of partially mineralized (**h**) and nonmineralized (**i**) tendons. Gold-labelled Phov (highlighted by red rectangles) were frequently found around and within the mineralized spherule. The yellow arrow indicates the intrafibrillar mineralization of collagen fibrils within the mineralized spherule (**h**). Gold particles and minerals were absent in the nonmineralized tendon (**i**). Scale bars: 200 nm. Experiments were repeated independently (**h**, **i**) three times with similar results.

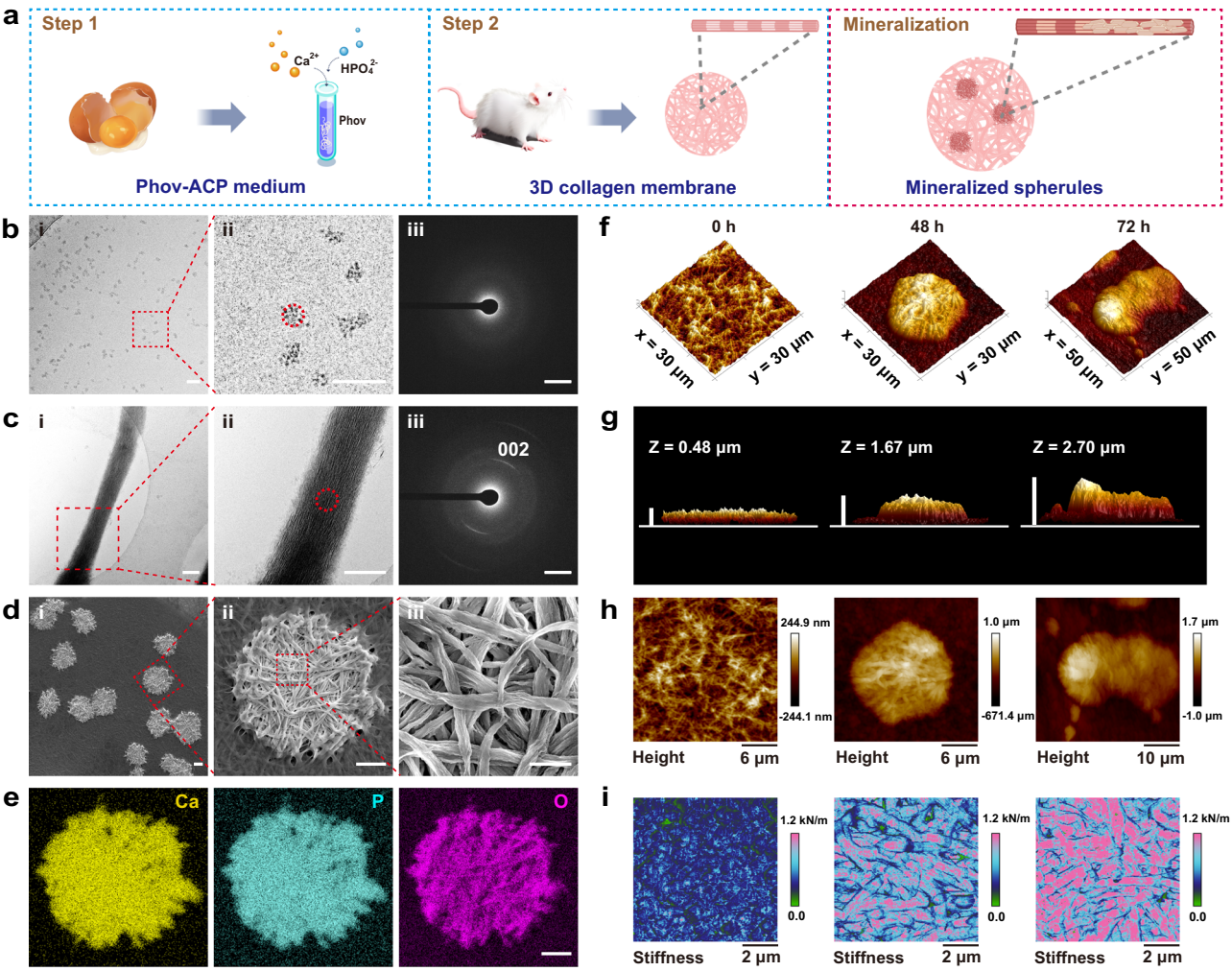

Fig. 2 | Characterization of the mineralized spherules induced by Phov-ACP. a Scheme of Phov-ACP preparation and collagen mineralization. Created in BioRender. Zhang, Y. (2024) https://BioRender.com/s17v456. **b** Cryo-TEM and SAED images of freshly prepared Phov-ACP complex. High-magnification image (**ii**) of the area indicated by the red rectangle in (**i**) showing discernible electron-dense granules (red circle). The SAED (**iii**) pattern of the area indicated by the red circle in (**ii**) validated the amorphous state of Phov-ACP. Scale bars: **i**, **ii** 50 nm; **iii** 2 1/nm. **c** Cryo-TEM and SAED images of a single collagen fibril that had been immersed in Phov-ACP for 24 h. High-magnification image (**ii**) showing a dense arrangement of needle-shaped mineral crystallites within the fibril. The SAED (**iii**) pattern of the area indicated by the red circle in (**ii**) showed (002) diffraction plane, indicating oriented apatite crystallites were aligned with the longitudinal axis of the fibril. Scale bars: **i**, **ii** 200 nm; **iii** 2 1/nm. **d** FIB-SEM images of the 3D collagen membrane after 48 h of mineralization by Phov-ACP. Mineralized spherules were evenly distributed within the collagen matrix. High-magnification images showed arrays of intrafibrillarly mineralized collagen fibrils constructed the mineralized spherules. Scale bars: **i**, **ii** 5 μm; **iii** 1 μm. Experiments were repeated independently (**b**–**d**) three times with similar results. **e** EDS elemental mapping of the area framed in (**d**–**ii**) showing the spatial distribution of calcium, phosphorus, and oxygen in the spherical inorganic-organic hybrid entity. Scale bar: 5 μm. **f**–**i** AFM measurement of nonmineralized 3D collagen membrane and samples that had been mineralized for 48 h and 72 h. 3D surface topography (**f**) combined with height images (**g**, **h**) of the spherules showed an increase in height. Stiffness maps (**i**) showed that the stiffness increased at mineral deposition sites as mineralization proceeded.

finding suggests that Phov can programme hierarchical orchestration from the nanoscale (mineralized collagen fibrils) to the mesoscale (mineralized spherules) in vitro.

These hierarchically mineralized structures were then characterized by atomic force microscopy (AFM) to measure their physical and mechanical properties, such as thickness and stiffness[18], during mineralization. 3D surface topography showed that within multi-layer collagen fibril membranes, mineralized spherules grew into hemispheric shapes with a height of 1.67 μm after 48 h. The thickness of the central region can reach up to 2.70 μm after 72 h (Fig. 2f–h). In addition, both intrafibrillar and extrafibrillar mineralization of collagen fibrils were observed in high-resolution TEM images after 72 h (Supplementary Fig. 6). This cross-fibrillar mineral deposition pattern may have contributed to the increase in the height of mineralized spherules. Furthermore, AFM stiffness maps illustrated that the stiffness of the collagen membrane improved as Phov-ACP-directed mineralization proceeded (Fig. 2i). Polarized light microscopy (PLM) was then used to evaluate the mineralization efficiency by monitoring the morphological development during crystallization[19]. As the PLM images showed, the average diameter of the mineralized spherules gradually increased from 4.65 ± 1.41 μm at 12 h to 34.99 ± 6.78 μm at 72 h (Supplementary Fig. 7a, b). These mineralized spherules continued to spread and progressively merged to form larger mineral aggregates of high crystallinity within 5 days (Supplementary Fig. 7). Based on the steady increase in mineral deposition, we demonstrated that Phov can guide mineralization with remarkable control and a distinct hierarchy in a highly efficient way, thus endowing materials with exceptional physical and mechanical properties in vitro.

Our findings provided an important clue that Phov, a highly phosphorylated natural NCP, could regulate the formation of mesoscale spherulitic building motifs by controllably mediating intrafibrillar mineralization. As reported, NCP analogues that mimic the functional domains of naturally occurring proteins can also achieve intrafibrillar mineralization of collagen fibrils[20,21]. However, it remains unclear whether mineralized spherules with cross-fibrillar mineralization could be feasibly induced by synthetic polyanionic or polycationic molecules via biomimetic strategies.

Phov-ACP-mediated mineralization is a highly biomimetic strategy

High-molecular-weight polyacrylic acid (HPAA) and polyallylamine hydrochloride (PAH) have the potential to modulate ACP phase transformation and CaP nucleation via their ionic charge (positive or negative)[22,23], promoting their wide applications in biomimetic mineralization. Accordingly, we used HPAA-stabilized ACP (4.5 mM Ca^{2+}, 2.1 mM HPO_4^{2-} and 150 μg/mL HPAA)[22] and PAH-stabilized ACP (4.5 mM Ca^{2+}, 2.1 mM HPO_4^{2-} and 150 μg/mL PAH)[23] as two types of mineralization media to decrypt how these agents modulate mineral deposition in the collagen matrix. Optical microscopy showed that compared with the control group (Phov-ACP mineralization medium), mineral growth induced by HPAA and PAH was randomly initiated and proceeded without order. Mineral morphologies in those two groups exhibited irregular patterns after 24, 48 and 72 h of mineralization (Supplementary Fig. 8). Although ultrastructural characterization by TEM and SEM confirmed intrafibrillar mineralization in the HPAA and PAH groups at 48 h, a typical spherulitic growth pattern of mineralization could not be observed at the micrometre scale (Fig. 3a–c and Supplementary Fig. 9). In contrast, Phov-ACP can not only mediate the formation of mineralized spherules within incompact reconstructed type I collagen matrix in vitro, but also direct the spherulitic mineralization pattern in compact connective tissues ex vivo, such as rat tail collagen fibres and nonmineralized turkey tendons (Fig. 3d, e and Supplementary Fig. 10). Besides, ex vivo mineralization models, characterized by FIB-SEM and 3D reconstruction, demonstrated that Phov-ACP could induce cross-fibrillar mineral deposition pattern within collagen matrix, thereby giving rise to the formation of mineralized spherules (Supplementary Fig. 11). Such Phov-mediated mineral growth pattern is strikingly similar to that in the early stage of physiological mineralization models in vivo (as we found), such as mouse incisor dentin, growing foetal mouse calvaria, and calcified turkey gastrocnemius tendon (Fig. 3f–h). Recently, a number of studies have demonstrated how biomacromolecules can be used to mineralize collagen matrices hierarchically[19,24,25]. From the well-aligned enamel rods to the hierarchically structured bone tissue, the importance of biomacromolecules in directing these highly organized mineralized structures in vitro has been underscored. Phov, a natural NCP, was found to have a remarkable capability to direct hierarchical mineralization on the mesoscale. This discovery holds promise for further advancing highly biomimetic mineralization strategies for hard tissue repair.

Given that synthetic polyelectrolytes, which mimic the net charge of NCPs, could not programme the formation of mesoscale mineralized spherules as Phov does under our experimental conditions, we speculated that NCPs modulate the structural hierarchy of the mineralized zone via another unknown underlying mechanism, which might not be limited to their negatively charged phosphorylated nature.

Conformational changes in phosvitin contribute to hierarchical mineralization

To elucidate how Phov controls mineral deposition within the organic matrix, 3D collagenous models, including multi-layer collagen fibril membranes and collagen scaffolds, were used as collagen matrices in vitro. Immunofluorescence staining and 3D reconstruction were utilized to identify the spatial correlation between calcium-rich spherule propagation and Phov precipitation within the collagen matrix (Fig. 4b). It was revealed that regions of calcified collagen in an ellipsoidal shape coincided with Phov deposition after 3 days of mineralization (Fig. 4c and Supplementary Movie 2). Likewise, CLSM provided high-resolution images of the presence of Phov at the initial calcification sites and in the densely packed mineralized spherules (Fig. 4e). These observations suggested that Phov binds to the collagen matrix and thereby spatially controls the progression of collagen-based hierarchical mineralization.

Fourier transform-infrared spectroscopy (FTIR) was then performed to probe the potential interactions between Phov-ACP and the collagen matrix. Collagen scaffolds immersed in Phov-ACP mineralization medium for designated time periods were prepared. For comparison, collagen scaffolds soaked in Phov solution without adding calcium and phosphate ions were used as the control group. A clear vibration band shown in the lyophilized Phov-ACP-collagen complex group at approximately 3200 cm^{-1} was assigned to N-H bond stretching[26] (Fig. 4f). This band is indicative of the hydrogen bond strength, which might contribute to the binding of Phov-ACP to collagen fibrils during mineralization. Analysis of the ratio of ν_3 PO_4 (mineral) to amide I (collagen) absorbances[27] showed that the degree of collagen mineralization was significantly increased as mineralization proceeded ($P = 0.0135$) (Fig. 4g). To further decrypt the interplay between Phov-ACP and collagen fibrils, the conformational changes in the secondary structure of the complex during mineralization were evaluated through decomposition of the amide I band at 1600–1720 cm^{-1}. The major structural elements were analysed, including aromatic ring vibrations, β-sheets, random coils, α-helices and turns[28] (Supplementary Table 1). Interestingly, the β-sheet content of the Phov-ACP-mediated mineralized collagen scaffolds steadily increased over 72 h compared with that of the control groups (Fig. 4h). Thus, Phov might undergo a conformational change into β-sheet structures under certain mineral concentrations, possibly binding with the collagen matrix and further spatially controlling the growth of mineralized spherules.

https://doi.org/10.1038/s41467-025-57189-8

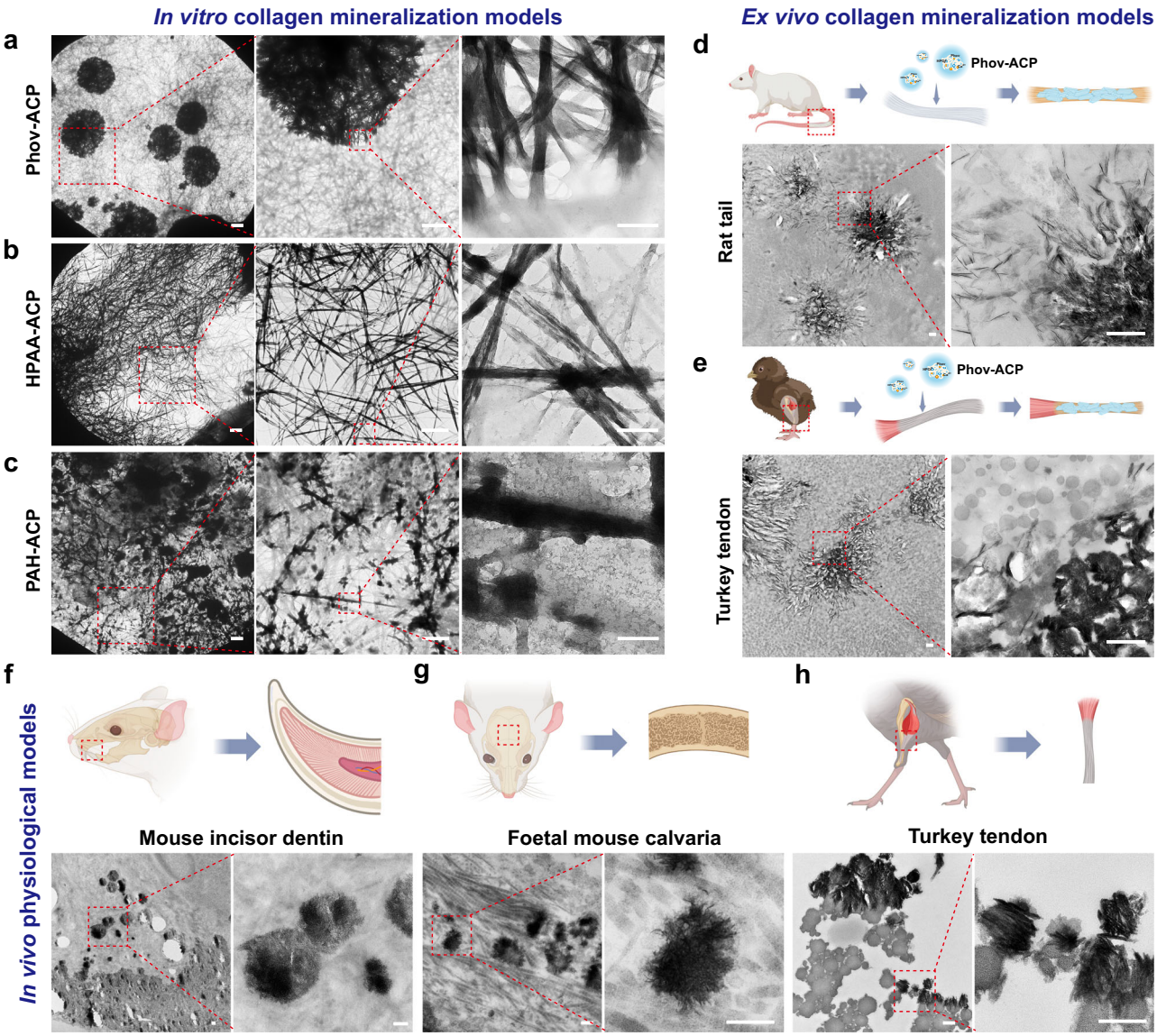

Fig. 3 | Mineral growth in in vitro, ex vivo, and in vivo mineralization models. **a**–**c** TEM images of the mineral deposition patterns on collagen fibril membranes that were immersed in Phov-ACP (**a**), HPAA-ACP (**b**), and PAH-ACP (**c**) solutions for 48 h. Red rectangles indicate the regions that are magnified in high-magnification images. Scale bars: 5 µm, 3 µm, and 500 nm (from left to right). **d**, **e** Schemes and TEM images of fibrous connective tissues (collagen tendons) mineralized by Phov-ACP for 72 h. Rat tail tendons (**d**) and unmineralized gastrocnemius tendons derived from 8-week-old turkeys (**e**) were used as ex vivo mineralization models. High-magnification images of the area indicated by the red rectangles showing the formation of mineralized spherules. Scale bars: 500 nm. **f**–**h** Schemes and TEM images of physiological mineralization models, including incisor dentin of 5-day-old mice (**f**), developing calvaria of foetal mice at embryonic age of E18 (**g**), and partially mineralized gastrocnemius tendon of 20-week-old turkeys (**h**). An analogous spherulitic growth pattern can be clearly observed within these collagen matrices. Scale bars: 200 nm. Experiments were repeated independently (**a**–**h**) three times with similar results. Schemes were partially created in BioRender. Zhang, Y. (2024) https://BioRender.com/j57a092.

As an intrinsically disordered phosphoprotein, Phov can adopt a β-sheet conformation under external stimuli[11]. Nevertheless, it remains unclear how calcium and phosphate ions at physiological concentrations induce conformational changes in Phov and how these conformational properties regulate hierarchical collagen-based mineralization.

Phov-ACP self-assembles into mineral-dense amyloid-like aggregate as a mesoscale mineralization template

To gain in-depth knowledge of Phov conformational changes after binding with calcium and phosphate ions, fluorescence spectroscopy was used for characterization. Tryptophan residues, which are positioned near the phosphorylated sequences of Phov[29,30], are sensitive fluorescent indicators[31]. Adding a series of concentrations of calcium and phosphate ions (molar ratio of Ca/P = 1.67) to Phov (75 µg/mL) contributed to a slight blueshift and a decrease in fluorescence intensity (Supplementary Fig. 12a). This indicated that the tryptophan residues were shielded from the solvent when the mineral ions bound to the phosphorylated residues of Phov[32], resulting in a conformational transition. The Stern–Volmer plot for the quenching of tryptophan fluorescence[32] showed that the intensity was not affected when the concentration of calcium ions was above 3.5 mM, indicating that the calcium-binding sites on Phov were saturated (Supplementary Fig. 12b). A thioflavin-T (ThT) fluorescence assay[33,34] was then used to monitor the formation of β-sheet-rich structures such as amyloid fibrils in Phov-ACP (Supplementary Fig. 13). ThT analysis revealed a significant time-dependent increase in the fluorescence intensity of Phov-ACP compared with the control group (Phov in tris buffer) ($P < 0.0001$). This indicated that in the presence of calcium and

https://doi.org/10.1038/s41467-025-57189-8

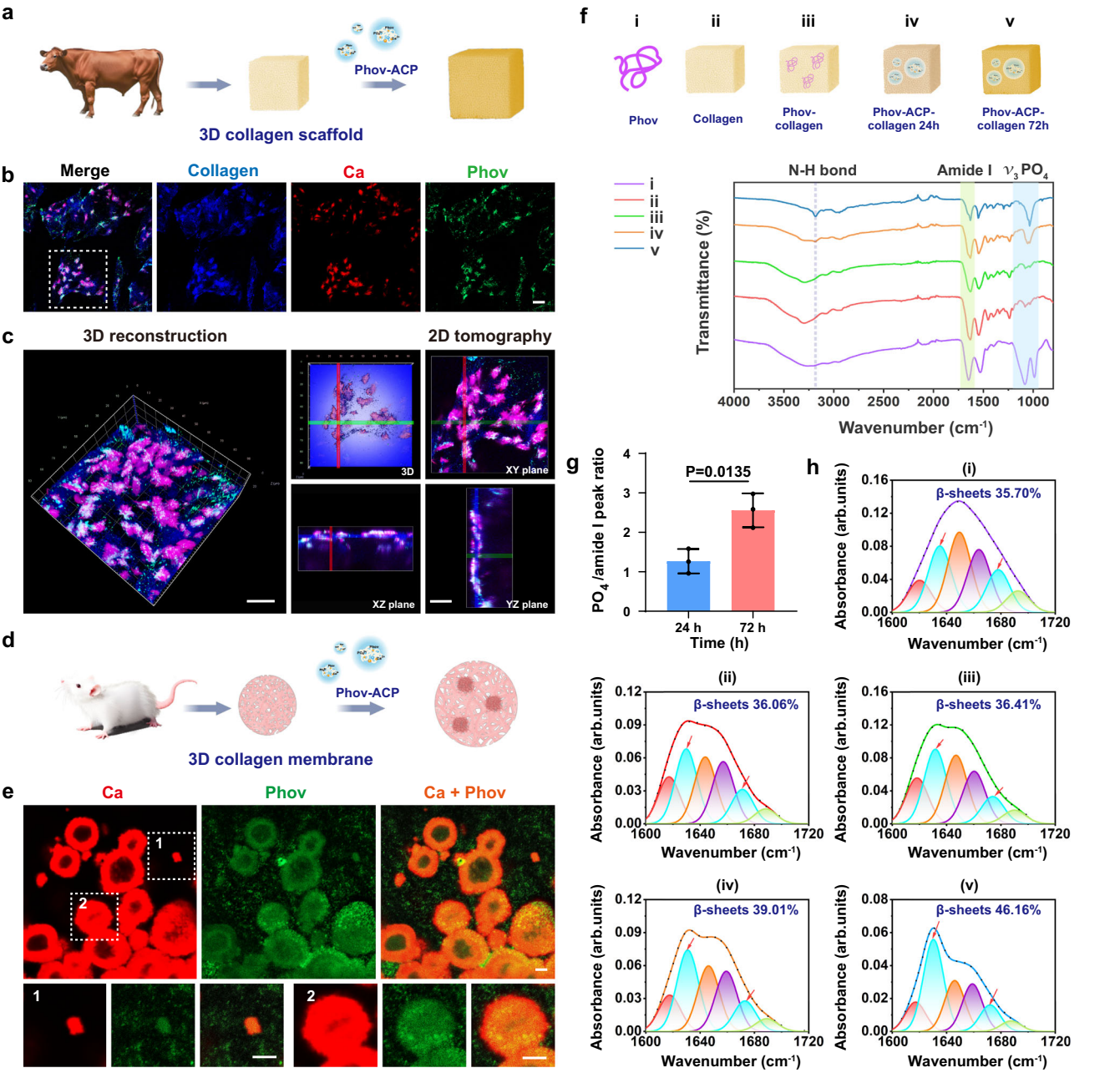

Fig. 4 | Phov-ACP directs hierarchical collagen-based mineralization through conformational changes. a Scheme showing the mineralization of 3D collagen scaffolds by Phov-ACP. **b** Immunofluorescence staining of bovine Achilles tendon-derived collagen scaffold, which had been mineralized by Phov-ACP for 72 h. Phov (green) was deposited at calcium-rich spherules (red) within the collagen scaffold (blue). Scale bar: 20 μm. **c** 3D reconstruction image and 2D tomography images of the mineralized area indicated by the white rectangle in (**b**). Ellipsoidal minerals surrounded by Phov could be clearly visualized in multiple orthogonal planes (XY, XZ, and YZ planes). Scale bars: 20 μm. **d** Scheme showing the mineralization of collagen membrane by Phov-ACP. Created in BioRender. Zhang, Y. (2024) https://BioRender.com/k93s017. **e** CLSM images showing the colocalization of Phov (green) and mineralized spherules (red) after 72 h of mineralization on a collagen membrane. The white rectangles highlight the mineralization sites at the early stage (**e**–**1**) and the late stage (**e**–**2**) of mineralized spherule formation. Scale bars: 10 μm. Experiments were repeated independently three times with similar results. **f** Scheme and FTIR spectra of pure Phov (**i**), pristine collagen (**ii**), Phov-collagen mixture (**iii**), and collagen mineralized by Phov-ACP for 24 h (**iv**) and 72 h (**v**). Peaks at 900 - 1200 cm^{-1}, 1600 - 1720 cm^{-1}, and 3200 cm^{-1} were assigned to the vibrations of the ν_3 PO$_4$ band, the amide I band and the N-H stretching band, respectively. **g** Quantification of the mineralization degree of the collagen scaffolds that were mineralized by Phov-ACP for 24 and 72 h. Data are presented as mean ± SD, $n = 3$ biologically independent samples, and two-tailed unpaired t-test (the P-value is shown). The difference with a P-value < 0.05 is considered significant. **h** Curve fitting analysis of the amide I band from the data in (**f**). The red arrow indicates the peaks for β-sheets. The dotted lines indicate the raw data. The coloured curve lines indicate the fitted data. The assignments of the FTIR vibrational bands for protein secondary structures are given in Supplementary Table 1.

phosphate clusters, Phov undergoes a constant conformational transition into amyloid-like fibrils.

To depict the morphological transitions of the Phov-ACP complex in a near-native environment, cryo-TEM combined with SAED was used to capture the structures of the complex through a quick cryofixation of the sample at different time points (0, 24 and 72 h). Supersaturated CaP solutions without Phov were used as controls. The freshly prepared Phov-ACP complexes were electron-dense nanoparticulates with

https://doi.org/10.1038/s41467-025-57189-8

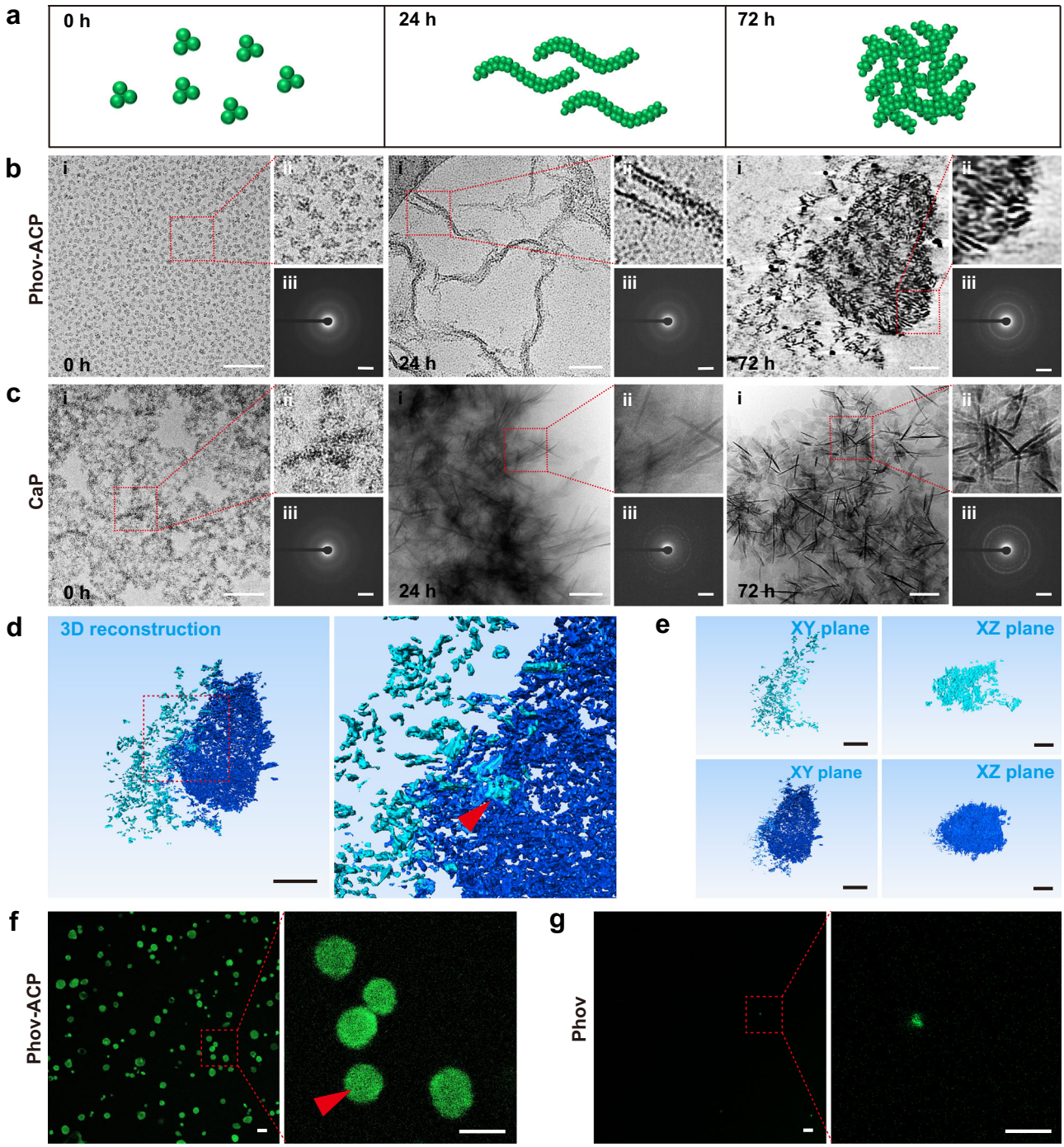

Fig. 5 | Phov-ACP assembled into mineral-dense amyloid-like aggregates. **a** Scheme of Phov-ACP self-assembly over time. **b**, **c** Cryo-TEM images and SAED patterns of Phov-ACP (**b**) and CaP solution (**c**) at designated time points (0, 24, 72 h). Scale bars: **i**, **ii** 100 nm; **iii** 2 1/nm. **d** 3D reconstruction of an electron tomography tilt series of Phov-ACP at 72 h in (**b**). High-magnification image (right) of the area indicated by the red rectangle showing entangled amyloid-like fibrils (red arrowhead). Scale bars: 200 nm. **e** 3D volume segmentation of Phov-ACP. Amyloid-like nanofibrils (cyan) and densely aggregated assemblies (blue) are shown in the XY plane and XZ plane views. Scale bars: 200 nm. **f**, **g** CLSM images of ThT-stained Phov-ACP (**f**) and Phov solution (**g**) after 72 h of incubation. The red arrowhead indicates roundish amyloid-like aggregates (green). Scale bars: 5 μm. Experiments were repeated independently (**b**, **c**, **f**, **g**) three times with similar results.

a diameter of approximately 10 nm in the amorphous phase (Figs. 2b and 5b). After 24 h of incubation, large quantities of amyloid-like nanofibrous entities that contained amorphous nanoparticulates could be clearly observed. After 72 h, aggregates comprising multiple ACP granules or needle-shaped nano-HAP crystals were formed (Fig. 5b). 3D reconstruction of cryo-TEM tomography images further revealed the amyloid-like nanofibrils entangled and dynamically assembled to form an aggregate with a diameter on the hundred nanometre-scale (Fig. 5d, e and Supplementary Movie 3). While in the control group, CaP particles coalesced randomly into branched assemblies at 0 h. Over time, the CaP clusters precipitated into a needle-like morphology at 24 h, and gradually transformed into plate-like apatite crystals over 72 h (Fig. 5c). CLSM images with ThT staining further confirmed that many roundish amyloid-like aggregates were present in Phov-ACP medium after 72 h of incubation (Fig. 5f). In contrast, these aggregates could not be found in the control group

(Phov in tris buffer) (Fig. 5g). Besides, small- and wide-angle X-ray scattering (SAXS and WAXS) analyses demonstrated that Phov-ACP is capable of self-assembling into amyloid-like aggregates (Supplementary Fig. 14). Furthermore, condensed calcium and phosphate ions were found inside the aggregates, as revealed by elemental mapping analysis (Supplementary Fig. 15).

These findings unveiled the morphological evolution and the progressive conformational transformation of Phov-ACP from initially evenly scattered ACP nanoparticles to self-assembled mineral-bearing amyloid-like aggregates. Conformational and structural changes endow proteins with the ability to guide crystal growth into distinctive hierarchical structures[35]. For example, proteins in the shape of amyloid-like nanoribbons induce enamel formation[14,36,37]. Identification of the conformational organization of Phov-ACP prompted us to explore whether amyloid-like aggregates are responsible for programming collagen-based mineralization into mineralized spherules at the mesoscale.

TEM was used to characterize the collagen mineralization process in the presence of Phov-ACP over 0 h, 24 h and 72 h. In the Phov-ACP medium, freshly prepared nanometre-sized clusters were found to adhere to the collagen fibrils at 0 h (Fig. 6a). Surprisingly, various entangled amyloid-like nanofibrils had assembled into spherical aggregates as early as 24 h during mineralization (Supplementary Fig. 16), and these mineral-rich aggregates with well-defined roundish morphology were closely bound to collagen fibrils (Fig. 6b). ACP granules released from the aggregates were found inside the fibrils, which are indicative of the initial mineralization sites. After 72 h of mineralization, the collagen fibrils were intrafibrillarly and extrafibrillarly mineralized, giving rise to the mineralized spherules, which were covered with amyloid-like aggregates (Fig. 6c and Supplementary Fig. 17). In the control group (CaP solution without Phov), only extrafibrillar mineralization could be observed after 24 and 72 h as the needle-like apatite randomly precipitated on the collagen fibrils (Fig. 6d–f).

Based on these observations, we surmised that the self-assembly of Phov-ACP into amyloid-like aggregates plays an essential role in templating the formation of the spherical inorganic–organic entities on the mesoscale. The aggregate serves as a mineralization template, providing a local mineral-dense network that loads inorganic mineral precursors of high concentration. The binding of amyloid-like aggregates to collagen fibrils accelerates collagen mineralization. In addition, fluorescence staining with amyloid-specific ThT fluorescence dye and CLSM also provided strong evidence that the binding of amyloid-like aggregates to the collagen matrix occurs not only in the avian tendon mineralization model in vivo but also in mineralized spherule formation mediated by Phov-ACP in vitro (Fig. 6g, h and Supplementary Fig. 18). Thus, self-assembled amyloid-like aggregates may spatially regulate the hierarchical mineralization of collagen fibrils into well-defined spherical hybrid entities.

Mechanism underlying the self-assembly of Phov-ACP

Biomacromolecules have distinct functional domains for regulating mineralized structures. Researchers have proposed that the functional domains of amelogenin are composed of hydrophobic and polar phosphorylated residues[37]. These domains enable its self-assembly into amyloid-like nanoribbons, thereby providing a conceptual scaffold for oriented HAP formation[38,39].

Interestingly, the C-terminal domain from residues Asp-195 to Phe-220 of Phov is also composed of a hydrophilic negatively charged sequence (DDSSSSSSSS), as well as an adjacent hydrophobic region with aliphatic-aromatic-rich side chains (VLSKIWGRHEIYQYRF)[30]. To verify whether such a combination of these two domains of Phov is the key functional segment for ACP stabilization and self-assembly, the aforementioned Phov-derived peptide was then synthesized and used to react with the supersaturated CaP solution. TEM combined with SAED showed that the peptide stabilized CaP into fibrous entities composed of amorphous electron-dense nanoparticles after 48 h post-preparation (Supplementary Fig. 19). STEM-EDS elemental mapping further confirmed that the distribution of peptide-derived nitrogen overlapped not only with the fibrous entities but also with the deposition of calcium and phosphorus (Supplementary Fig. 20). This indicates that the peptide can stabilize ACP (Peptide-ACP) and self-assemble into a fibrillar structure under the influence of mineral ions. Furthermore, TEM combined with negative staining and ThT fluorescence assays also provided evidence that compared with the control group (peptide in tris buffer), introducing mineral ions to the peptides resulted in an increasing formation of β-sheets and mature fibril-like structures (Supplementary Figs. 21, 22). These findings suggest that mineral ions enhance the self-assembly of key functional segments of Phov into amyloid-like fibrils.

Delving into the intricacies of the functional peptide of Phov in mineralization can offer important insights into the role of full-length Phov in ACP stabilization and conformational transformation during the collagen mineralization process. Therefore, Phov-derived functional segments were then used in molecular dynamics (MD) simulations to predict and analyse the formation of amyloid-like Phov-ACP at the atomic level. The conformational states of pristine β-sheets from the peptide subsegments were prebuilt, and their stability was evaluated after calcium and phosphate ions were introduced into the system (Fig. 7a and Supplementary Fig. 23)[39,40]. The β-sheet conformations, especially in the hydrophobic region, remain relatively stable due to intermolecular hydrogen bonding between the backbones (Fig. 7b–e and Supplementary Movie 4). Ionic dense precursor clusters[41,42] comprising calcium and phosphate ions were preferentially found near the negatively charged side chains, which adopted a relatively flexible conformation in solution (Fig. 7b). The simulation revealed that the Coulombic interactions between calcium cations and acidic residues predominantly mediated such interaction, which attenuated the repulsion between adjacent peptides (Fig. 7f). The decreased electrostatic repulsion helped stabilize and condense the β-sheet conformations in the peptides (Fig. 7g). Consequently, these observations provided strong evidence that peptide chains from the C-terminal domain of Phov as monomers could not only stabilize ACP precursors but also self-fold into a β-sheet structure.

Interestingly, the simulation revealed that increasing the number of mineral-containing single β-sheets to the simulation system caused single β-sheets to further aggregate to form cross-β-sheet structures[43] (Fig. 7h, i). Based on the binding energy calculation, van der Waal's forces or hydrophobicity should be involved in the formation of cross-β-sheets (Fig. 7j). In particular, hydrophobic interactions between tryptophan and phenylalanine residues from individual single-β-sheets (π-π stacking of the aromatic rings) facilitate the formation of hydrophobic interfaces, which are buried within cross-β-sheet structures (Fig. 7k and Supplementary Fig. 24). Meanwhile, hydrophilic acidic side chains with multiple deposited ACP droplets are more flexible and disordered and protrude into the solution (Fig. 7l and Supplementary Fig. 25). This unique self-assembled cross-β-sheet structure is consistent with the cryo-TEM observation in which electron-dense ACP granules were orderly deposited around the axis of the amyloid-like fibril (Figs. 5b, 7m). Subsequently, amyloid-like fibrils continue to assemble into mineral-dense aggregates, which spatially bind with collagen fibrils and release ACP droplets for hierarchical collagen mineralization on the mesoscale. However, elucidating the involvement of Phov-ACP amyloid-like aggregates in modulating mineralized spherule formation should consider the contribution of Phov-ACP in directing intrafibrillar mineralization at the nanoscale. Mineralized collagen fibrils serve as nanoscale structural motifs within mesoscale spherical building blocks. It remains unclear how Phov-ACP aggregates bind to collagen fibrils as well as how ACP particles are released from these

https://doi.org/10.1038/s41467-025-57189-8

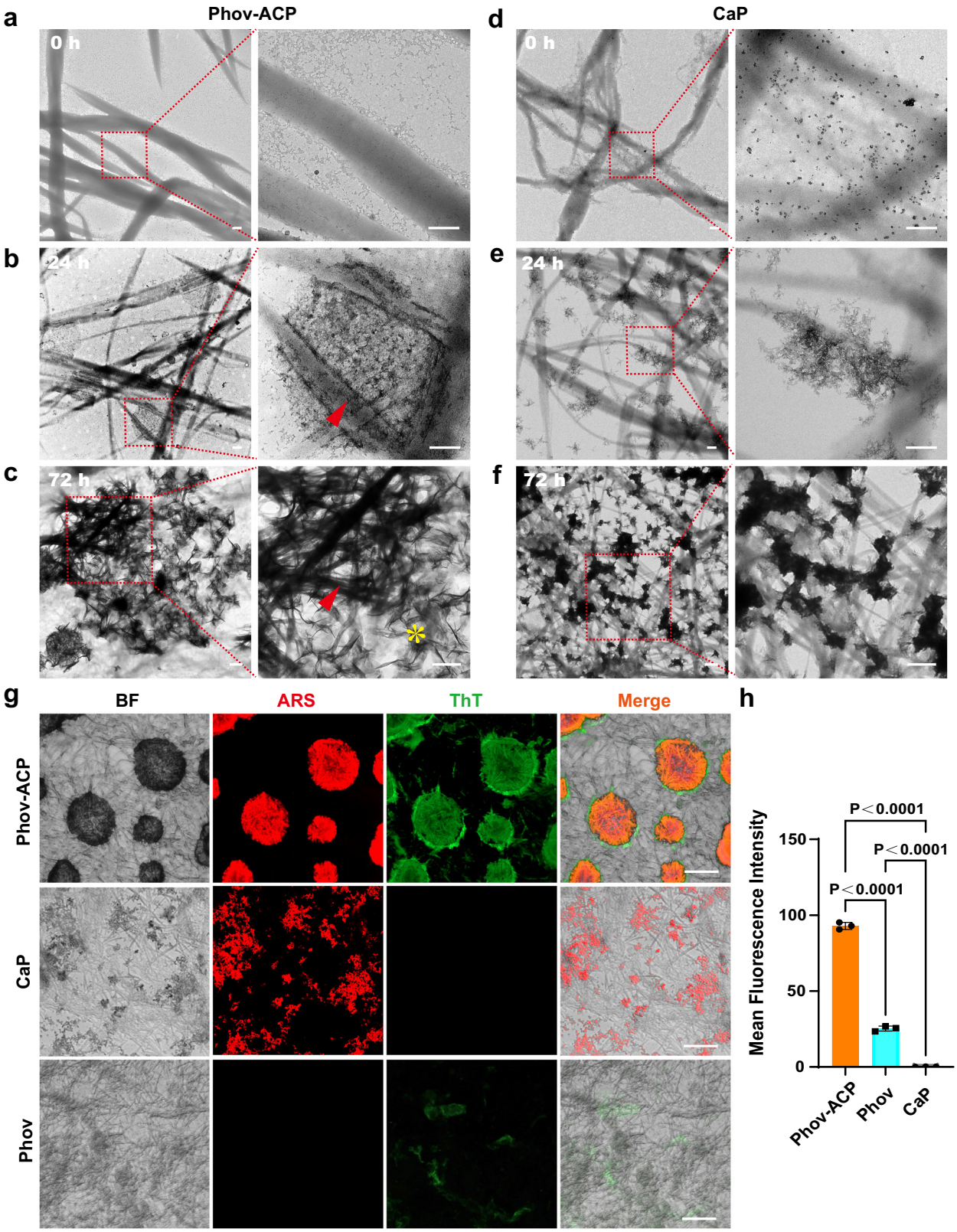

complexes and subsequently diffuse into the collagen fibrils for intrafibrillar mineralization at the nanoscale.

Mechanism underlying Phov-ACP-induced intrafibrillar mineralization on the nanoscale

To investigate the Phov-ACP binding sites on collagen fibrils, the ultrastructure of the collagen fibrils in the early stage of mineralization was evaluated via cryo-TEM combined with uranyl acetate staining. Cryo-TEM image revealed that Phov-ACP complexes with electron-dense nanofibrous structures were randomly attached to the collagen fibril after 6 h of mineralization (Fig. 8a). Different from the synthetic anionic polyelectrolytes, Phov is a natural NCP which is composed of both positively and negatively charged domains, enabling it to interact with charged groups on collagen fibrils[44]. Thus, Phov and Phov-ACP

Fig. 6 | Mineral-dense amyloid-like aggregates regulate the formation of mineralized spherules at the mesoscale. **a**–**c** TEM images of collagen fibrils mineralized by Phov-ACP for 0 h (**a**), 24 h (**b**) and 72 h (**c**). **a** Nanometre-sized clusters adhered to the unmineralized collagen fibrils. **b** Mineral-dense amyloid-like aggregates bound to collagen fibrils. The red arrowhead indicates the ACP infiltrated into the collagen fibrils. **c** A spherical structure comprising intrafibrillarly mineralized collagen fibrils (red arrowhead) and plate-like extrafibrillar crystallites (yellow asterisk). Scale bars: **a**, **b** 200 nm; **c** 1 µm. **d**–**f** TEM images of collagen fibrils immersed in CaP solution without Phov for 0 h (**d**), 24 h (**e**) and 72 h (**f**). **d** Minerals were randomly deposited outside the collagen fibrils. **e** Needle-like mineral motifs aggregated into irregular assemblies, attaching to the surface of collagen fibrils. **f** Crystalline apatite formed without order and precipitated on the collagen fibrils. Scale bars: **d**, **e** 200 nm; **f** 1 µm. **g** Bright field and CLSM images of collagen fibrils immersed in Phov-ACP (top), CaP (middle) or Phov solution (bottom) after 48 h. ThT fluorescence showed amyloid-like aggregates bound to mineralized spherules in the Phov-ACP group. In the control groups (CaP and Phov), the ThT signal could hardly be observed. Green, ThT for amyloids; red, ARS for minerals; BF, bright field. Scale bars: 20 µm. **h** Analysis of ThT fluorescence intensities in different groups. Data are presented as mean ± SD, $n = 3$ biologically independent samples, one-way analysis of variance (ANOVA) followed by Tukey's multiple comparison test (the P-values are shown). Differences with P-values < 0.05 are considered significant.

have strong binding affinities for collagen fibrils and bind along these fibrils (Supplementary Fig. 26).

MD simulation was subsequently employed to clarify the binding mechanism between Phov-ACP and collagen fibrils. After 100 ns of simulation, the Peptide-ACP further self-assembled into a more condensed structure that could bind to collagen (Supplementary Fig. 27a, b, f, g). By calculating the binding energy between the peptides and collagen, Coulombic attraction and van der Waal's forces, including hydrogen bonds, were revealed to be involved in binding (Supplementary Fig. 27c–e). The binding of Phov-ACP to collagen, which is stimulated by multiple driving forces, may increase the concentration of mineral precursors around the fibrils. Further analysis demonstrated that ACP precursors were released from the Peptide-ACP complex and adhered to the collagen, which was driven by Coulombic attraction between the mineral clusters and the collagen (Supplementary Fig. 28).

The Phov-ACP complexes are negatively charged, as demonstrated by zeta potential analysis (Supplementary Fig. 29). According to the concept of electrostatic interaction theory, negatively charged ACP can be attracted to positively charged regions of collagen in the gap zone (such as a-band)[45]. However, a time-resolved study of a single collagen fibril mineralized by Phov-ACP revealed that ACP infiltrated into both the gap zone and the overlap zone of the fibril after 12 h of mineralization (Fig. 8b). The infiltration of ACP into the overlap zone indicates that besides the aforementioned short-ranged electrostatic interaction, other long-ranged driving forces for intrafibrillar mineralization may be involved. Given that Phov (34 kDa) in the presence of mineral ions self-assembled into amyloid-like nanofibrous entities, the overall molecular weight and net charge of the entity increased, resulting in growing electrochemical potential and osmotic pressure between the extrafibrillar and intrafibrillar compartments[23,46,47]. Based on the Gibbs–Donnan equilibrium theory[48], the balance between osmotic equilibrium and electroneutrality may also be responsible for ACP diffusion into collagen fibrils.

Once ACP enters the fibril, its transformation into apatite crystals subsequently occurs. It is still unknown whether Phov infiltrates into the fibrils, thereby directing crystal nucleation. CLSM combined with 3D reconstruction was then used to visualize the spatial distribution of Phov and minerals within collagen fibrils after 48 h mineralization. High-resolution images showed the fluorescently labelled Phov was excluded from the fibrils, while the minerals were deposited inside the collagen (Supplementary Fig. 30). This indicates that the self-assembly process of Phov increases its molecular weight, potentially contributing to its inability to penetrate the fibrils due to size exclusion effect[49]. In addition, our findings also support the notion that collagen is capable of inducing the transformation of ACP to apatite without the involvement of NCPs for nucleation[45,50].

In biomineralization, in addition to Phov, multiple phosphorylated IDPs have been immunolocalized at the mineralization front[10], but their potential role in regulating hierarchical mineralization from the mesoscale to the nanoscale has never been elucidated. Our findings provide evidence that the amphiphilic nature of these intrinsically disordered phosphorylated proteins might accelerate the conformational transition under external stimuli to a self-assembled mineral-containing template on the mesoscale; in this process, one acidic domain stabilizes inorganic ACP, while another domain interacts with other organic interfaces, such as collagen fibrils. At the nanoscale, Coulombic attraction and van der Waal's forces between Phov-ACP and collagen fibrils facilitate their binding process. Such binding promotes the release of mineral precursors from Phov-ACP complexes. The electrostatic interactions, Gibbs–Donnan equilibrium, and size exclusion effect may contribute to the infiltration of these ACP precursors into the collagen for intrafibrillar mineralization, while Phov remains outside the fibril, further regulates mineral deposition in extrafibrillar space. The collagen fibrils involved in Phov-ACP-mediated mineralization function as a matrix scaffold for mineral deposition and crystallization.

Interestingly, the process by which Phov templates mesoscale spherical entities to mineralize the collagen matrix of hard tissues is strikingly similar to honeybees constructing hexagonal honeycombs to expand hives. The Phov assembly with a distinct shape may act as a transmitter that releases ACP droplets and as a template that spatially regulates the morphology of hierarchical mineralization from the nanoscale to the mesoscale (Fig. 8d). The astonishing homogeneity of such totally unrelated natural behaviours sheds light on the intrinsic essence of nature's architectural hierarchy.

In summary, we have shown that Phov, a highly phosphorylated IDP, is an ingenious architect capable of precisely orchestrating collagen-based hierarchical mineralization. From mesoscale mineralized spherules to nanoscale cross-fibrillar mineralization, Phov replicates the hierarchical mineralization pattern in vitro and ex vivo. The highly negatively charged nature of Phov enables the stabilization of ACP, and the hydrophobic segments of Phov dominate the self-assembly and aggregation processes. These factors contribute to Phov-stabilized ACP self-assembly into mineral-dense amyloid-like aggregates, which serve as mineralization templates that spatially regulate the formation of mineralized spherules on the mesoscale. Deep into the nanoscale, the Phov-ACP complex binds to collagen driven by Coulombic attraction and van der Waal's forces. ACP precursors subsequently diffuse and infiltrate into collagen fibrils for intrafibrillar mineralization, in which the electrostatic interactions, the Gibbs–Donnan equilibrium, and the size exclusion effect may be involved. However, it is elusive whether these mechanisms can apply to other functional peptides, even from different phosphoproteins, for hierarchical mineralization. Besides, the molecular mechanisms also need further exploration, as the current MD simulation is limited in the accessibility of large time and length scales of full-length Phov-ACP interaction, as well as spatial and temporal resolution of intrafibrillar nucleation events. Implementing enhanced sampling techniques and improving algorithmic efficiency will optimize the MD simulation and provide more concrete evidence in future work. The precise control of Phov in directing mesoscale structural motifs represents a highly biomimetic mineralization strategy, which is promising to endow materials with exquisite structural designs and exceptional physical properties. Thus, this discovery may offer valuable approaches for highly biomimetic hard tissue repair, particularly for bone and dentin regeneration.

https://doi.org/10.1038/s41467-025-57189-8

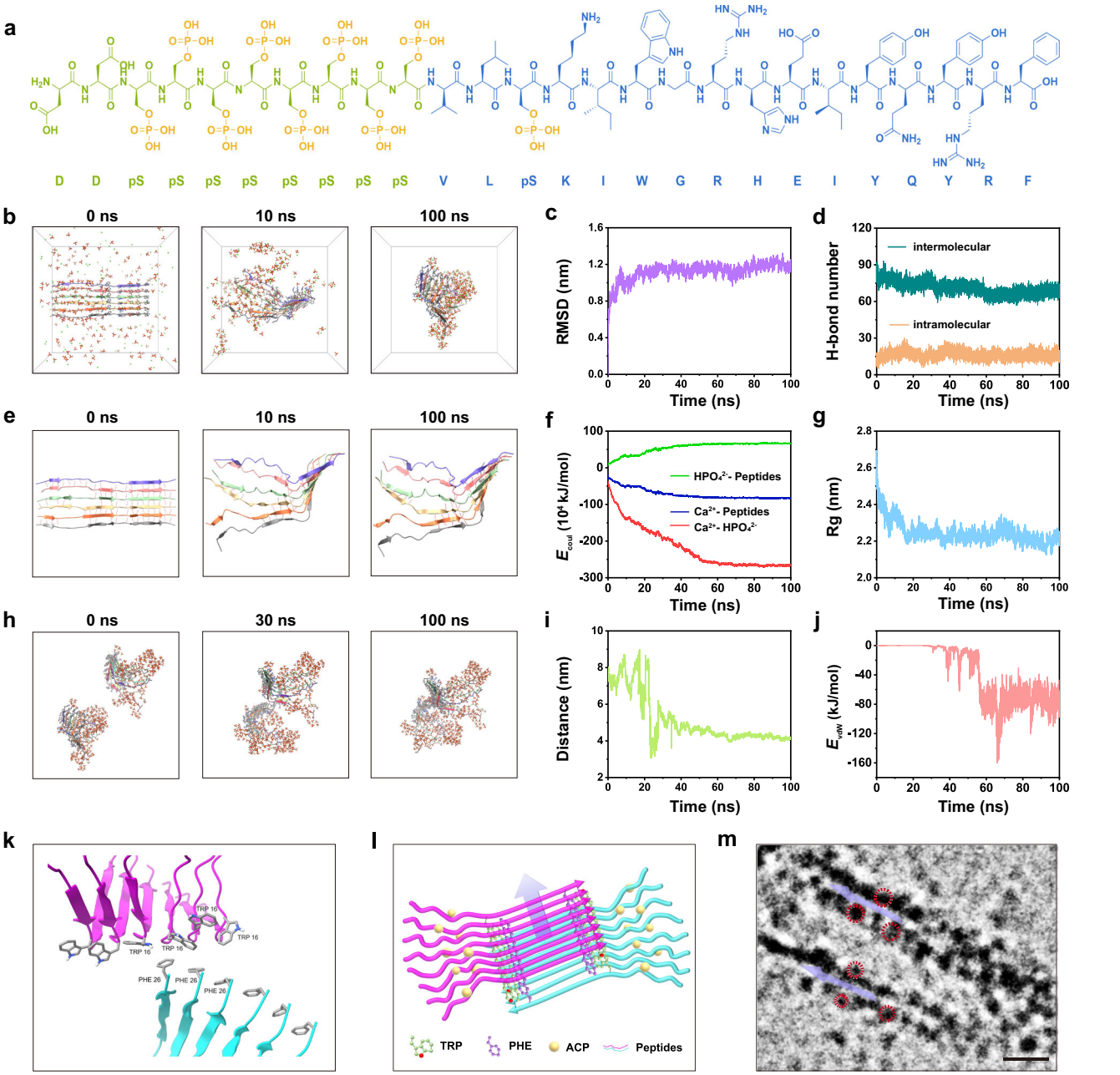

Fig. 7 | Molecular dynamics simulations of the mechanism of Phov-ACP self-assembly. a Monomer peptide from the C-terminal domain of Phov (Asp-195 to Phe-220). **b** Snapshots showing the binding of calcium and phosphate ions (ACP) to peptide subsegments. Pristine single β-sheets (six peptide monomers) were prebuilt and simulated in TIP3P water at pH 7.4. **c** Root mean square deviation (RMSD) plot for the conformational stability of β-sheets until 100 ns. **d** Intermolecular and intramolecular hydrogen bond (H-bond) numbers in β-sheets ($t = 100$ ns). **e** Molecular dynamics simulation trajectories of six Phov peptide monomers at times $t = 0$, 10, and 100 ns. The intermolecular H-bonds (red dotted lines) in the hydrophobic region contribute to the stable β-sheet configuration. **f** Coulomb energy (E_{coul}) of Ca^{2+}-peptides, HPO_4^{2-}-peptides, and Ca^{2+}-HPO_4^{2-}. **g** Radius of gyration (Rg) versus time plot during the 100 ns simulation for pristine β-sheets. Rg analysis showed that the β-sheets became more compact when ACP bound to the negative hydrophilic domain. **h** Snapshots showing two individual β-sheets loaded with ACP self-assembled into a cross-β-sheet structure. **i** Variations in the centroid distance of two individual β-sheets. **j** Van der Waal's energy (E_{vdw}) is favourable for the binding of two individual β-sheets. **k** Snapshot view of the binding sites between two individual β-sheets. An intermolecular association between Phe and Trp could be observed. **l** Scheme of the Phov-ACP structure with a cross-β-sheet conformation. Hydrophilic acidic side chains from Phov stabilize ACP droplets (yellow globules) and protrude into the solution. The hydrophobic domain facilitates the formation of hydrophobic interfaces (purple arrow), which are shielded from the solvent. **m** Cryo-TEM image showing the amyloid-like nanofibrous assembly of Phov-ACP at 24 h (high-magnification image of Fig. 5b). The red dashed circles indicate the electron-dense ACP nanoparticulates. The purple arrows indicate the hydrophobic gaps. Scale bar: 50 nm.

Methods

Ethics statement

This research was conducted in line with the National Institute Guide for the Care and Use of Laboratory Animals. All animal experiments were approved by the Institutional Animal Care and Use Committee (IACUC), ZJCLA (approval No. ZJCLA-IACUC-20010324).

Materials

Phosvitin (Phov), with a molecular weight of 34 kDa and a phosphorus content of 8–10%, was purchased from Sigma-Aldrich. Except as mentioned afterward, all of the chemicals we utilized were of analytical grade or higher and were obtained from Sigma-Aldrich.

https://doi.org/10.1038/s41467-025-57189-8

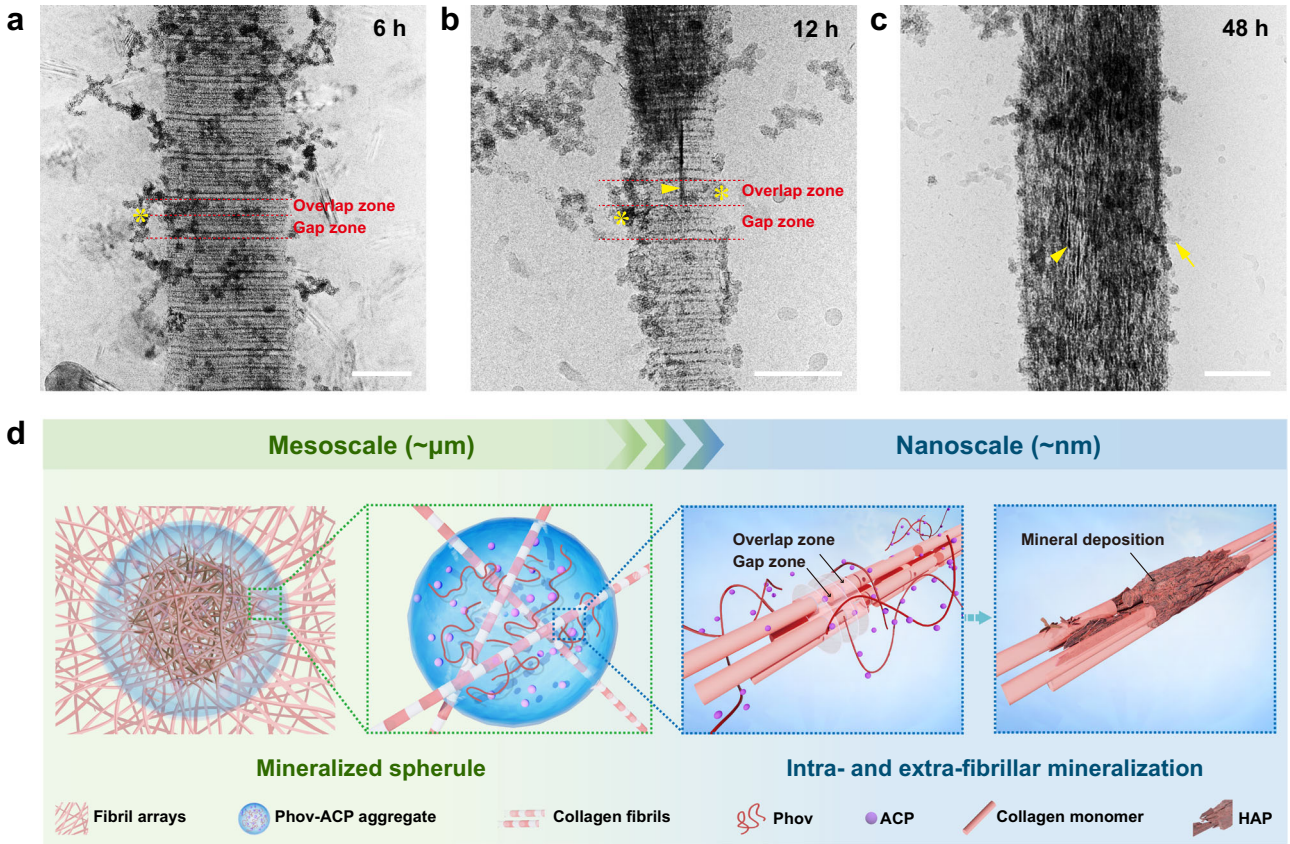

Fig. 8 | Phov-ACP mediates intra- and extra-fibrillar mineralization. a Cryo-TEM image of a uranyl acetate stained collagen fibril mineralized by Phov-ACP for 6 h. Phov-ACP with an electron-dense nanofibrous structure (asterisk) randomly bound to the collagen. **b** A stained collagen fibril mineralized for 12 h. ACP (asterisks) infiltrated into the fibril without a discernible preference for band location. Needle-like apatite (arrowhead) could be observed within the intrafibrillar space. **c** After 48 h of mineralization, the collagen fibril was highly mineralized, with intrafibrillar apatite crystallites (arrowhead) aligned along the fibril's *c*-axis and extrafibrillar crystalline (arrow) deposited around the fibril. Scale bars: 100 nm. Experiments were repeated independently (**a**–**c**) three times with similar results. **d** Schematic overview of Phov-mediated hierarchical mineralization. On the mesoscale, Phov-ACP self-assembles into mineral-dense amyloid-like aggregates and spatially binds to the collagen matrix, thereby regulating the mineralized spherule formation and growth. On the nanoscale, Phov-stabilized ACPs adhere to the collagen fibrils. Driven by multiple forces, ACPs are released from Phov and diffuse into the fibril, resulting in collagen intra- and extra-fibrillar mineralization. The precise regulation from the nanoscale cross-fibrillarly mineralized collagen fibrils into the mesoscale mineralized spherules lies in the intricate Phov-mediated hierarchical orchestration. Abbreviation: Phov, phosvitin; ACP, amorphous calcium phosphate; HAP, hydroxyapatite.

Specimen preparation

Foetal C57BL/6 J mice at embryonic age of E18 ($n = 3$), 5-day-old C57BL/6 J mice ($n = 3$), and 2-month-old Sprague–Dawley rats ($n = 6$) with both sexes were purchased from the Zhejiang Centre of Laboratory Animals. Legs from Standard Bronze turkeys with both sexes at 8-week-old ($n = 21$), 20-week-old ($n = 21$) and 26-week-old ($n = 3$) were collected from a local farm (Xinmiao Farm). All of the animals were euthanized before the surgical procedure. The mandible incisors of 5-day-old mice, the calvaria of foetal E18 mice, and the gastrocnemius tendons of turkey legs were carefully dissected from adjacent tissues with a scalpel. Dissection was conducted in an ice bath with phosphate-buffered saline (PBS) solution. The samples were then fixed in 2.5% glutaraldehyde or 4% paraformaldehyde for further characterization.

Mineralization medium preparation

Tris (hydroxymethyl) aminomethane (tris) buffer was prepared as follows: 150 mM NaCl, 8 mM Tris-base, and 42 mM Tris-HCl were added to 100 mL of deionized water, and the pH was adjusted to 7.4 with 3 M HCl. $CaCl_2{\cdot}2H_2O$ and K_2HPO_4 were added to tris buffer to obtain a 7.0 mM Ca^{2+} stock solution and a 4.2 mM HPO_4^{2-} stock solution, respectively. A certain amount of Phov was added to the Ca^{2+} stock solution and then blended with an equal volume of 4.2 mM HPO_4^{2-} solution to obtain a Phov-stabilized amorphous calcium phosphate (Phov-ACP) mineralization medium. The final solution contained 75 μg/mL Phov, 3.5 mM Ca^{2+}, and 2.1 mM HPO_4^{2-}. Partially phosphorylated Phov-derived peptide (DDSSSSSSSSVLSKIWGRHEIYQYRF) was synthesized and purified by Sangon Biotechnology Co. Ltd. Peptide-stabilized ACP (Peptide-ACP) was prepared using the same method. The final solution contained 1 mg/mL peptide, 3.5 mM Ca^{2+}, and 2.1 mM HPO_4^{2-}.

High-molecular-weight polyacrylic acid (HPAA) stabilized ACP (HPAA-ACP) and polyallylamine hydrochloride (PAH) stabilized ACP (PAH-ACP) were prepared as follows: a certain amount of HPAA (Mw: 450 kDa) or PAH (Mw: 15 kDa) was added to the 9.0 mM Ca^{2+} stock solution, and mixed with an equal volume of 4.2 mM HPO_4^{2-} solution, respectively. The final HPAA-ACP solution[22] contained 150 μg/mL HPAA, 4.5 mM Ca^{2+} and 2.1 mM HPO_4^{2-}. The final PAH-ACP solution[23] contained 150 μg/mL PAH, 4.5 mM Ca^{2+} and 2.1 mM HPO_4^{2-}.

Reconstruction of self-assembled collagen matrices

Type I collagen fibres were freshly dissected from the tails of 2-month-old Sprague–Dawley rats with both sexes ($n = 3$) and dissolved in 0.3 M acetic acid to obtain a 12 mg/mL collagen stock solution. Self-assembled collagen fibrils were reconstructed from the collagen stock solution according to a dialysis method[51]. Briefly, the self-assembled collagen fibrils were obtained by placing the collagen stock

solution in a dialysis bag surrounded by PBS solution (pH 7.4) at 37 °C. The self-assembled collagen fibril solution was then diluted to 0.1-1.0 mg/mL, dropped onto glass slides or grids, and air-dried to prepare single collagen fibril models, single-layer collagen fibril membrane models, and multi-layer collagen fibril membrane models.

Mineralization experiments

For mineralization in vitro, glass slides coated with reconstructed self-assembled collagen membranes and the 3D collagen scaffolds (ACE Surgical Supply Co.) were immersed in Phov-ACP solution and incubated for the designated time periods. The grids coated with self-assembled collagen fibrils were turned upside down and floated on the Phov-ACP solution for mineralization.

For mineralization ex vivo, type I collagen fibres dissected from the tails of 2-month-old Sprague–Dawley rats with both sexes ($n = 3$) and nonmineralized turkey gastrocnemius tendons obtained from 8-week-old Standard Bronze turkeys with both sexes ($n = 3$) were cut into $2 \times 2 \times 2$ mm^3 sections and mineralized in Phov-ACP solution for 72 h.

Micro-computed tomography (micro-CT) analysis

Tendons were scanned using a high-resolution micro-CT scanner (MILabs, U-CT-XUHR) at 50 kV and 0.21 mA. IMALYTICS Preclinical (version 2.1.8.9) was used to reconstruct the projection images. Mineralization fronts (i.e., transition regions between the mineralized and nonmineralized portions) were identified at the proximal end of the partially mineralized tendons, which were distinct due to the significant difference in radiographic density between the mineralized and nonmineralized portions.

Histological and immunofluorescence staining

For histological staining, tendons near the mineralization front were embedded in paraffin wax blocks. Tendons were then cut into 6 µm thick sections and stained with haematoxylin & eosin (H&E) and von Kossa to visualize the structure of the tissues and the potential mineral deposition.

For alizarin red S (ARS) staining, the tendon slices mineralized by Phov-ACP ex vivo were incubated in 2% ARS solution for 10 min to label the minerals. After ARS staining, the specimens were rinsed with deionized water for 10 min prior to examination.

For immunofluorescence staining, fresh tendons were sectioned at 8 µm thickness with a cryomicrotome (Leica CM3050S). The sections were blocked with goat serum and then incubated with primary antibody solutions, including collagen type I polyclonal antibody (14695-1-AP, Proteintech) and monoclonal antibody phosvitin (D-5) (sc-46681, Santa Cruz Biotechnology) overnight. The sections were then incubated with secondary antibody solutions, including goat anti-mouse IgG H&L (Alexa Fluor® 488) and goat anti-rabbit IgG H&L (Alexa Fluor® 647). The sections were then stained with ARS to label calcium deposition, and stained with 4,6-diamidino-2-phenylindole (DAPI) to label nuclei. The specimens were observed with a confocal laser scanning microscope (CLSM) (Zeiss LSM980). For both of the non-mineralized and partially mineralized groups, images of six different specimens from each group were obtained at the same magnification for semiquantitative immunofluorescence analysis. Measurements and calculations of relevant fluorescence intensities were performed using the ImageJ software (version 2.0.0). For immunofluorescence staining of 3D collagen scaffolds and multi-layer collagen membranes after mineralization, collagen, Phov and calcium deposition were labelled with the same reagents.

FITC-labelled Phov (FITC-Phov) was synthesized by Sangon Biotechnology Co. Ltd and utilized to prepare a FITC-Phov-stabilized ACP medium for collagen mineralization. Immunofluorescence staining of the mineralized collagen fibrils was conducted using the same reagents previously mentioned for staining collagen and minerals.

Immunogold electron microscopy (immunogold-EM)

Sample preparation for immunogold labelling was conducted following established protocols[52]. Briefly, tendon sections were fixed in a mixture of 4% formaldehyde and 0.1% glutaraldehyde at 4 °C for 4 h. Tendon slices were then dehydrated with an ascending ethanol series, and embedded in LR Gold resin (London Inc.). Leica UC7 microtome was used to prepare ultrathin sections (70 nm). For immunogold labelling, the monoclonal antibody phosvitin (D-5) was used as the primary antibody, and IgG-conjugated gold particles (10 nm in diameter, Sigma-Aldrich) were used as the secondary antibody. The sections were visualized using a Talos L120C microscope (Thermo Scientific) at 120 kV.

Cryogenic transmission electron microscopy (cryo-TEM) and 3D tomography

For observation of collagen fibril mineralization, Quantifoil Jena R2/2/gold grids with a coating of single-layer collagen fibrils were floated upside down on the Phov-ACP solution for designated time periods. Mineralized collagen fibrils with or without 15 seconds of 0.5% uranyl acetate staining were vitrified and observed by a Talos F200C microscope (FEI, Hillsboro) at 200 kV, with an exposure setting of approximately 20 e/Å^2.

To observe the morphology of Phov-ACP, gold grids were surface plasma-treated prior to use. Phov-ACP solution or CaP solution was dropped onto the grids. The grids were vitrified and examined with a Talos F200C microscope. Selected area electron diffraction (SAED) was applied to measure the crystallinity of the calcium phosphate minerals. For size analysis, cryo-TEM images were analysed with ImageJ software[53]. The size distribution of Phov-ACP particles was statistically measured by counting at least 200 randomly selected particles in the captured images. A histogram of particle diameter was generated using Origin 2021 software.

For electron tomography, the samples were tilted in 3° steps from approximately 50° to −50° using the SerialEM 3.8 software package. The collected tomograms were aligned with the IMOD package. Further 3D volume segmentation and rendering were carried out by Amira software (version 2019.1).

Transmission electron microscopy (TEM) and scanning electron microscopy (SEM)

To investigate the microstructure of physiologically mineralized tissues, tendon sections from 20-week-old Standard Bronze turkeys with both sexes ($n = 3$), mandible incisors from 5-day-old C57BL/6 J mice with both sexes ($n = 3$) and the calvaria from foetal E18 mice with both sexes ($n = 3$) were fixed in 2.5% glutaraldehyde. The samples were embedded in epoxy resin, and sliced at a 120 nm thickness. After staining with 4% uranyl acetate and lead citrate, the ultrathin slices were visualized using a Talos L120C microscope at 120 kV.

To characterize the microscopic structure of Phov, Phov-ACP, Peptide, Peptide-ACP and CaP, the samples were incubated for the designated time points, dropped onto the grids, and examined via TEM with or without 2% uranyl acetate staining for 2 min.

To investigate the mineral deposition patterns of different mineralization media (Phov-ACP, CaP, HPAA-ACP and PAH-ACP), single-layer collagen fibrils mineralized for the designated time periods were examined via TEM. For SEM, the slides coated with mineralized multi-layer collagen fibril membranes were sputter-coated with gold. The surface morphology of the samples was imaged with a FEI Nova NanoSEM 450 (Thermo Fisher) at 5 kV.

Focused ion beam-SEM (FIB-SEM) and energy dispersive X-ray spectroscopy (EDS)

The grids covered with multi-layer collagen fibril membranes were mineralized with Phov-ACP solution for 48 h. FIB Helios G3 UC (Thermo Fisher) with an ICD detector was utilized in backscatter mode,

with an acceleration voltage of 5 kV and a current of 0.1 nA. For 3D reconstruction of mineralized spherules formed in ex vivo models, the samples were prepared with a slice thickness of 10 nm and imaged in sequence[54]. The serial images were reconstructed using Amira software (version 2019.1). EDS was performed to measure the calcium and phosphorus contents and to obtain the corresponding elemental spatial distribution mapping of the mineralized spherules.

Scanning transmission electron microscopy (STEM) and EDS mapping

Grids coated with single-layer collagen fibril membranes were floated upside down over the Phov-ACP solution for the designated time periods. The samples were imaged with an FEI Nova NanoSEM 450 (Thermo Fisher) in STEM mode. EDS mapping was performed to visualize the elemental spatial distribution of the Phov-ACP aggregates and the mineralized collagen fibrils. The elemental distribution of Peptide-ACP after 48 h post-preparation was examined by STEM-EDS mapping using the same method.

Atomic force microscopy (AFM)

Glass slides covered with multi-layer collagen membranes were mineralized with Phov-ACP solution for designated time periods. The physical and mechanical properties of the mineralized spherules were measured by PeakForce quantitative nanomechanical mapping (PeakForce-QNM) using Dimension Icon AFM (Bruker). A RTESPA-525 Tip with a nominal spring constant of 200 N/m and a tip with a curvature radius of 30 nm was used to detect the samples, with a scan rate of 0.6 Hz. The surface morphology and stiffness distribution of the samples were further analysed by NanoScope Analysis (version 1.90, Bruker).

Mineralization efficiency assessment

Glass slides coated with multi-layer collagen membranes were mineralized with Phov-ACP solution for a series of designated time periods. Optical microscopy (Leica DM2000) was utilized to observe the growth pattern and morphological changes of the mineralized spherules during the mineralization process. The size distribution of mineralized spherules was analysed with ImageJ[53]. At each designated time point, at least 70 particles from captured images of each sample were randomly selected for calculation. Each group consisted of three biologically independent samples. The degree of mineralization was assessed by the coverage of the mineralized region.

Polarized light microscope (Eclipse E600POL, Nikon) was used to observe the birefringence change of the mineralized spherules, which indicated the transformation from an amorphous state to a crystalline state[19].

Attenuated total reflectance-Fourier transform infrared spectroscopy (ATR-FTIR)

Three-dimensional collagen scaffolds were mineralized with Phov-ACP solution (75 μg/mL Phov, 3.5 mM Ca^{2+} and 2.1 mM HPO_4^{2-}) for 24 h and 72 h, while the pure Phov powder, bare collagen scaffold, and the collagen scaffolds soaked in Phov solution (75 μg/mL Phov) without calcium and phosphate ions were served as control groups. All of the samples were freeze-dried in advance. Infrared spectra between 400 ~ 4000 cm^{-1} were obtained using a Nicolet iS50FT-IR spectrophotometer (Thermo Scientific) equipped with an ATR setup, with a resolution of 4 cm^{-1} and 32 scans. Peaks at 900 ~ 1200 cm^{-1}, 1600 ~ 1720 cm^{-1} and 3200 cm^{-1} were assigned to the vibrations of ν_3 PO_4 band, amide I band and N-H stretching band, respectively[27–29]. The degree of mineralization of the collagen matrix was assessed by the band area ratio of ν_3 PO_4 to the amide I band absorbance[28]. Curve-fitting analysis of the amide I band was performed to estimate the relevant proportions of the major components representing secondary structures using Peakfit software (version 4.12)[29]. The assignments of the FTIR vibrational bands for the secondary structures are given in Supplementary Table 1.

Fluorescence spectroscopy

A series of Phov-CaP solutions containing 75 μg/mL Phov and different concentrations of CaP (molar ratio of $[Ca^{2+}]/[HPO_4^{2-}] = 3.5$: 2.1) were prepared, including: i) Phov (75 μg/mL); ii) Phov-CaP containing Ca^{2+} 0.87 mM and HPO_4^{2-} 0.52 mM; iii) Phov-CaP containing Ca^{2+} 1.75 mM and HPO_4^{2-} 1.05 mM; iv) Phov-CaP containing Ca^{2+} 3.5 mM and HPO_4^{2-} 2.1 mM; and v) Phov-CaP containing Ca^{2+} 5.25 mM and HPO_4^{2-} 3.15 mM. Fluorescence spectroscopy was performed at 25 °C with a JASCO FP-8550 spectrofluorometer. Spectra were recorded with an excitation wavelength of 278 nm and an emission wavelength ranging from 200 to 500 nm. Both the excitation and emission slit widths were 5 nm. Fluorescence spectra were normalized by subtracting the signal from pure tris buffer. The Stern–Volmer equation was used to calculate fluorescence quenching[32].

$$\frac{FI_0}{FI} = \frac{\tau_0}{\tau} = 1 + K_{sv} \cdot Q \tag{1}$$

In the formula, FI_0 represents the fluorescence intensity of 75 μg/mL Phov, and FI represents the fluorescence intensity of Phov-CaP solutions with different concentrations of CaP. τ_0 and τ are the lifetimes of Phov with and without Cap, respectively. K_{sv} is the Stern–Volmer constant.

CLSM combined with thioflavin-T (ThT) staining

Amyloid-specific fluorescence dye (ThT) was used to detect the presence of amyloid-like aggregates in the partially mineralized avian tendon in vivo and in the mineralized collagen matrix in vitro. The samples were stained with 0.1 mg/mL ThT solution for 10 min and then stained with ARS for 10 min at room temperature. The samples were examined by CLSM (Zeiss LSM980), and the ThT mean fluorescence intensities were measured by ImageJ.

To detect the presence of amyloid-like aggregates in the Phov ACP solution at 72 h post-preparation, the samples were stained with 0.1 mg/mL ThT solution for 10 min. Phov in tris buffer served as the control group. All samples were observed using CLSM at an excitation wavelength of 488 nm.

ThT fluorescence assay

To monitor the conformational transition of Phov upon the introduction of mineral ions, 2 μL of ThT solution (1 mM) was mixed with 200 μL of Phov-ACP, or 200 μL of Phov solution (as the control group), respectively. The samples were measured by a fluorescence spectrophotometer (Horiba, iHR550) with excitation at 440 nm and emission at 484 nm. Three replicates were conducted for each group. The ThT fluorescence intensities of Peptide-ACP solution and Peptide solution (as the control group) were examined using the same method.

Small- and wide-angle X-ray scattering (SAXS and WAXS)

SAXS and WAXS experiments were carried out using the XEUSS 3.0 beamline (XENOCS, France) that employs the excillum METALJET liquid metal jet X-ray source and Dectris EIGER2 Si 1 M detector. Operational parameters were set at 70 kV, 3.5 mA, and 250 W, with each measurement lasting 600 seconds. After subtracting the normalized background, the data were analysed in terms of the scattered intensity, $I(q)$, as a function of the magnitude of the scattering vector, q. SAXS and WAXS data analysis was performed using the Fit2D software.

Zeta potential analysis

The zeta potentials of Phov, Phov-ACP, and CaP were measured using a Zetasizer Nano ZS90. The electrophoretic light scattering method was utilized to assess the zeta potential of charged particles in solution,

with the measurements conducted at a temperature of 25 °C and a voltage of 50 V.

Molecular dynamics (MD) simulation

MD simulations of the Phov-ACP formation process and their interactions with the collagen membrane were performed using the GROMACS 2021.5 package[55]. Phov-derived key functional segments (sequence: DDSSSSSSSSVLSKIWGRHEIYQYRF)[30] with a prebuilt pristine β-sheet structure were modelled by UCSF ChimeraX software[56] and the CHARMM-GUI website[57]. HPO_4^{2-} ions and the peptides were parameterized by the CHARMM36 force field[58]. Ca^{2+} ions were parameterized by the HFE parameter set for the TIP3P water model developed by Li/Merz[59]. All simulation results were visualized using UCSF ChimeraX software.

To evaluate the dynamics of the Phov-derived segments after introducing both calcium and phosphate ions to the system, a simulation box was constructed, extending at least 1.4 nm beyond the boundaries of the peptides ($11 \times 11 \times 11\ nm^3$). The system was solvated with TIP3P water at pH 7.4, and 152 particles of $CaHPO_4$ together with 0.15 M NaCl were introduced to keep electrical neutrality. The steepest descent method was conducted for energy minimization. After 1.0 ns NPT equilibration, an NPT MD simulation was performed for 100 ns at 310 K and 1 bar. The LINCS algorithm was employed to restrict the bond lengths of hydrogen atoms. The Particle Mesh Ewald (PME) approach, with a real-space cut-off of 12 Å, was utilized to evaluate the long-range electrostatic interactions. Lennard-Jones interactions were truncated at a 12 Å cut-off, applying a switching function beyond 10 Å. To analyse structural dynamics, the root mean square deviation (RMSD) and radius of gyration (Rg) of the Phov-derived segments were calculated. The aggregation behaviour of the Phov segment-ACP complex was also simulated, and the centroid distance between two Phov-ACP complexes was measured. Electrostatic and Lennard-Jones interactions in this process were calculated using the same methodologies.

The interaction between Phov-ACP and collagen was further simulated. To achieve equilibrium, a simplified collagen membrane, composed of the triple-helix segment of collagen type I (PDB: 7CWK)[60], underwent a 30 ns pre-simulation. The final size of the collagen membrane was $15.6 \times 15.6 \times 3.7\ nm^3$. Two individual Phov segment-ACPs were placed 2.0 nm away from the collagen membrane. The solvent conditions, as well as the ambient pressure and temperature, were kept consistent with previous simulations. An NPT MD simulation lasting 100 ns was conducted. The contact number between mineral ions (Ca^{2+} and HPO_4^{2-}) and the collagen membrane was calculated. Centroid distance, electrostatic interactions, and Lennard-Jones interactions were calculated using the same methods aforementioned.

Statistics and reproducibility

All experiments were performed at least three times independently. The quantitative data were presented as the mean ± standard deviation (SD). After confirming the assumptions of normality and homoscedasticity, parametric statistical methods were applied. Two-tailed unpaired *t*-tests were performed for two-group comparisons, and one-way or two-way analysis of variance (ANOVA) were used for multiple comparisons when more than two groups were compared, followed by Tukey's or Bonferroni's multiple comparison test. A value of $P < 0.05$ was considered statistically significant. All of the statistical analyses were performed with GraphPad Prism 9.0 software.

Reporting summary

Further information on research design is available in the Nature Portfolio Reporting Summary linked to this article.

Data availability

All data supporting the findings of this study are available within the article and the Supplementary Information Files. For Figs. 1g, 4f–h, 6h, 7c, d, f, g, i, j, and Supplementary Figs. 3, 4b, 7b, c, 12, 13,14, 18c, 22, 24, 27, 28, 29 in the associated source data file. All other data are available from the corresponding author upon request. Source data are provided in this paper.

References

1. Nepal, D. et al. Hierarchically structured bioinspired nanocomposites. *Nat. Mater.* **22**, 18–35 (2023).
2. Yip, S. & Short, M. P. Multiscale materials modelling at the mesoscale. *Nat. Mater.* **12**, 774–777 (2013).
3. Franklin, R., Niverty, S., Harpur, B. A. & Chawla, N. Unraveling the mechanisms of the *Apis mellifera* honeycomb construction by 4D X-ray microscopy. *Adv. Mater.* **34**, 2202361 (2022).
4. Free, R. et al. Mesoscale structural gradients in human tooth enamel. *Proc. Natl. Acad. Sci. USA* **119**, e2211285119 (2022).
5. Kashiwa, H. K. & Komorous, J. Mineralized spherules in the cells and matrix of calcifying cartilage from developing bone. *Anat. Rec.* **170**, 119–127 (1971).
6. Macías-Sánchez, E. et al. Spherulitic crystal growth drives mineral deposition patterns in collagen-based materials. *Adv. Funct. Mater.* **32**, 2200504 (2022).
7. Rodriguez-Palomo, A., Østergaard, M. & Birkedal, H. Bone hierarchical structure: heterogeneity and uniformity. *Adv. Funct. Mater.* **33**, 2307026 (2023).
8. Micheletti, C. et al. Bone mineral organization at the mesoscale: A review of mineral ellipsoids in bone and at bone interfaces. *Acta Biomater.* **142**, 1–13 (2022).
9. Zou, Z. et al. Three-dimensional structural interrelations between cells, extracellular matrix, and mineral in normally mineralizing avian leg tendon. *Proc. Natl. Acad. Sci. USA* **117**, 14102–14109 (2020).
10. George, A. & Veis, A. Phosphorylated proteins and control over apatite nucleation, crystal growth, and inhibition. *Chem. Rev.* **108**, 4670–4693 (2008).
11. Sarem, M. et al. Disordered conformation with low Pii helix in phosphoproteins orchestrates biomimetic apatite formation. *Adv. Mater.* **29**, 1701629 (2017).
12. Oldfield, C. J. & Dunker, A. K. Intrinsically disordered proteins and intrinsically disordered protein regions. *Annu. Rev. Biochem.* **83**, 553–584 (2014).
13. He, G., Dahl, T., Veis, A. & George, A. Nucleation of apatite crystals in vitro by self-assembled dentin matrix protein 1. *Nat. Mater.* **2**, 552–558 (2003).
14. Habelitz, S. & Bai, Y. Mechanisms of enamel mineralization guided by amelogenin nanoribbons. *J. Dent. Res.* **100**, 1434–1443 (2021).
15. Boskey, A. L. & Villarreal-Ramirez, E. Intrinsically disordered proteins and biomineralization. *Matrix Biol.* **52–54**, 43–59 (2016).
16. Fratzl, P., Kolednik, O., Dieter Fischer, F. & Dean, M. The mechanics of tessellations–bioinspired strategies for fracture resistance. *Chem. Soc. Rev.* **45**, 252–267 (2016).
17. Samaraweera, H., Zhang, W., Lee, E. & Ahn, D. U. Egg yolk phosvitin and functional phosphopeptides–review. *J. Food Sci.* **76**, R143–R150 (2011).
18. Krieg, M. et al. Atomic force microscopy-based mechanobiology. *Nat. Rev. Phys.* **1**, 41–57 (2019).
19. Elsharkawy, S. et al. Protein disorder-order interplay to guide the growth of hierarchical mineralized structures. *Nat. Commun.* **9**, 2145 (2018).
20. Oosterlaken, B. M., Vena, M. P. & de With, G. In vitro mineralization of collagen. *Adv. Mater.* **33**, 2004418 (2021).
21. Thrivikraman, G. et al. Rapid fabrication of vascularized and innervated cell-laden bone models with biomimetic intrafibrillar collagen mineralization. *Nat. Commun.* **10**, 3520 (2019).
22. Song, Q. et al. Contribution of biomimetic collagen-ligand interaction to intrafibrillar mineralization. *Sci. Adv.* **5**, eaav9075 (2019).

23. Jiao, K. et al. Complementarity and uncertainty in intrafibrillar mineralization of collagen. *Adv. Funct. Mater.* **26**, 6858–6875 (2016).
24. de Wildt, B. W. M. et al. Bioinspired silk fibroin mineralization for advanced in vitro bone remodeling models. *Adv. Funct. Mater.* **32**, 2206992 (2022).
25. Qin, D. et al. Rapid biomimetic mineralization of keratin scaffold via electrodeposition with potential for bone regeneration. *Eur. Polym. J.* **196**, 112322 (2023).
26. Brzeska, J. et al. Branched polyurethanes based on synthetic polyhydroxybutyrate with tunable structure and properties. *Polymers* **10**, 826 (2018).
27. Querido, W. et al. Fourier transform infrared spectroscopy of developing bone mineral: from amorphous precursor to mature crystal. *Analyst* **145**, 764–776 (2019).
28. Chadefaux, C., Le Hô, A.-S., Bellot-Gurlet, L. & Reiche, I. Curve-fitting micro-ATR-FTIR studies of the amide I and II bands of type I collagen in archaeological bone materials. *EPreserv. Sci.* **6**, 129–137 (2009).
29. Czernick, D., Liu, J., Serge, D. & Salih, E. Topographical distribution of phosphorylation sites of phosvitins by mass spectrometry. *J. Proteomics* **83**, 76–98 (2013).
30. Byrne, B. M. et al. Amino acid sequence of phosvitin derived from the nucleotide sequence of part of the chicken vitellogenin gene. *Biochemistry* **23**, 4275–4279 (1984).
31. Ghisaidoobe, A. B. T. & Chung, S. J. Intrinsic tryptophan fluorescence in the detection and analysis of proteins: a focus on Förster resonance energy transfer techniques. *Int. J. Mol. Sci.* **15**, 22518–22538 (2014).
32. Lakowicz, J. R. *Principles of Fluorescence Spectroscopy* (Springer Science & Business Media, 2013).
33. Arad, E., Green, H., Jelinek, R. & Rapaport, H. Revisiting thioflavin T (ThT) fluorescence as a marker of protein fibrillation-The prominent role of electrostatic interactions. *J. Colloid Interface Sci.* **573**, 87–95 (2020).
34. Xue, C., Lin, T. Y., Chang, D. & Guo, Z. Thioflavin T as an amyloid dye: fibril quantification, optimal concentration and effect on aggregation. *R. Soc. Open Sci.* **4**, 160696 (2017).
35. Levin, A. et al. Biomimetic peptide self-assembly for functional materials. *Nat. Rev. Chem.* **4**, 615–634 (2020).
36. Du, C., Falini, G., Fermani, S., Abbott, C. & Moradian-Oldak, J. Supramolecular assembly of amelogenin nanospheres into birefringent microribbons. *Science* **307**, 1450–1454 (2005).
37. Wang, D. et al. Controlling enamel remineralization by amyloid-like amelogenin mimics. *Adv. Mater.* **32**, 2002080 (2020).
38. Lin, T. J. & Heinz, H. Accurate force field parameters and pH resolved surface models for hydroxyapatite to understand structure, mechanics, hydration, and biological interfaces. *J. Phys. Chem. C* **120**, 4975–4992 (2016).
39. Akkineni, S. et al. Amyloid-like amelogenin nanoribbons template mineralization via a low-energy interface of ion binding sites. *Proc. Natl. Acad. Sci. USA* **119**, e2106965119 (2022).
40. Yang, Y., Cui, Q. & Sahai, N. How does bone sialoprotein promote the nucleation of hydroxyapatite? A molecular dynamics study using model peptides of different conformations. *Langmuir* **26**, 9848–9859 (2010).
41. Habraken, W. J. E. M. et al. Ion-association complexes unite classical and non-classical theories for the biomimetic nucleation of calcium phosphate. *Nat. Commun.* **4**, 1507 (2013).
42. Garcia, N. A. et al. Simulation of calcium phosphate prenucleation clusters in aqueous solution: Association beyond ion pairing. *Cryst. Growth Des.* **19**, 6422–6430 (2019).
43. Michaels, T. C. T. et al. Amyloid formation as a protein phase transition. *Nat. Rev. Phys.* **5**, 379–397 (2023).
44. Saxena, N. et al. Comparison of synthetic vs. biogenic polymeric process-directing agents for intrafibrillar mineralization of collagen. *Polymers* **14**, 775 (2022).
45. Nudelman, F. et al. The role of collagen in bone apatite formation in the presence of hydroxyapatite nucleation inhibitors. *Nat. Mater.* **9**, 1004–1009 (2010).
46. Wallace, E. W. J. et al. Reversible, specific, active aggregates of endogenous proteins assemble upon heat stress. *Cell* **162**, 1286–1298 (2015).
47. Chen, G. et al. Amyloid beta: structure, biology and structure-based therapeutic development. *Acta Pharmacol. Sin.* **38**, 1205–1235 (2017).
48. Niu, L. et al. Collagen intrafibrillar mineralization as a result of the balance between osmotic equilibrium and electroneutrality. *Nat. Mater.* **16**, 370–378 (2017).
49. Toroian, D., Lim, J. E. & Price, P. A. The size exclusion characteristics of type I collagen: Implications for the role of noncollagenous bone constituents in mineralization. *J. Biol. Chem.* **282**, 22437–22447 (2007).
50. Landis, W. J. & Silver, F. H. Mineral deposition in the extracellular matrices of vertebrate tissues: Identification of possible apatite nucleation sites on type I collagen. *Cells Tissues Organs* **189**, 20–24 (2008).
51. Shen, M. et al. MV-mimicking micelles loaded with PEG-serine-ACP nanoparticles to achieve biomimetic intra/extra fibrillar mineralization of collagen in vitro. *Biochim. Biophys. Acta Gen. Subj.* **1863**, 167–181 (2019).
52. Lv, M. F. et al. Improved quantification of immune-gold labeling and its use to compare the distribution of cellular factors among subchloroplast compartments. *Micron* **145**, 103060 (2021).
53. Debut, A. et al. Effect of visual cognition on the measurement of particle size using ImageJ software. *Curr. Mater. Sci. Former. Recent Pat. Mater. Sci.* **14**, 141–154 (2021).
54. Wang, X. Z. et al. Stage-specific and location-specific cartilage calcification in osteoarthritis development. *Ann. Rheum. Dis.* **82**, 393–402 (2023).
55. Abraham, M. J. et al. GROMACS: High performance molecular simulations through multi-level parallelism from laptops to supercomputers. *SoftwareX* **1–2**, 19–25 (2015).
56. Pettersen, E. F. et al. UCSF ChimeraX: Structure visualization for researchers, educators, and developers. *Protein Sci.* **30**, 70–82 (2021).
57. Choi, Y. K. et al. CHARMM-GUI nanomaterial modeler for modeling and simulation of nanomaterial systems. *J. Chem. Theory Comput.* **18**, 479–493 (2021).
58. Maier, J. A. et al. Ff14SB: improving the accuracy of protein side chain and backbone parameters from ff99SB. *J. Chem. Theory Comput.* **11**, 3696–3713 (2015).
59. Li, P., Roberts, B. P., Chakravorty, D. K. & Merz, K. M. Rational design of particle mesh Ewald compatible Lennard-Jones parameters for +2 metal cations in explicit solvent. *J Chem. Theory Comput.* **9**, 2733–2748 (2013).
60. Yan, J. et al. Calcified apoptotic vesicles from PROCR+ fibroblasts initiate heterotopic ossification. *J. Extracell. Vesicles* **13**, e12425 (2024).

Acknowledgements

We thank Jiansheng Guo and Lingyun Wu in the Centre of Cryo-Electron Microscopy (CCEM), Zhejiang University, for their technical assistance on FIB-SEM and cryo-TEM. This work was supported by the National Natural Science Foundation of China (81991500 and 81991502 to Q.M.C., 82301138 to M.J.S., 81970956 to M.J.W.), the National Key R&D Programme of China (2022YFC2402900 to Q.M.C.), and the Young Elite Scientists Sponsorship Programme by CAST (2022QNRC001 to M.J.S.).

Author contributions

M.J.S., C.Y.Z., and Y.Y.Z. contributed equally to this work. M.Q.Z. and Q.M.C. jointly supervised this work. M.J.S. designed the study. M.J.S., C.Y.Z., and Y.Y.Z. performed all experiments, collected data, and conducted statistical analysis. D.Y.L. and J.Y. participated in data analysis. M.J.S., C.Y.Z., and Y.Y.Z. wrote the manuscript and drew the figures. D.Y.L., J.Y., Z.Y.W., M.J.W., M.Q.Z., and Q.M.C. provided advice and contributed to manuscript revision. All authors approved the submitted version of the manuscript.

Competing interests

The authors declare no competing interests.

Additional information

Supplementary information The online version contains supplementary material available at https://doi.org/10.1038/s41467-025-57189-8.

Correspondence and requests for materials should be addressed to Mengqi Zhu or Qianming Chen.

Peer review information *Nature Communications* thanks the anonymous reviewers for their contribution to the peer review of this work. A peer review file is available.